DEFENSE TECHNICAL INFORMATION CENTER

Information for the Defense Community

DTIC® has determined on Month 09 Day 23 Year 2008 *that this Technical Document has the Distribution Statement checked below. The current distribution for this document can be found in the DTIC® Technical Report Database.*

☒ **DISTRIBUTION STATEMENT A.** Approved for public release; distribution is unlimited.

☐ © **COPYRIGHTED.** U.S. Government or Federal Rights License. All other rights and uses except those permitted by copyright law are reserved by the copyright owner.

☐ **DISTRIBUTION STATEMENT B.** Distribution authorized to U.S. Government agencies only. Other requests for this document shall be referred to controlling office.

☐ **DISTRIBUTION STATEMENT C.** Distribution authorized to U.S. Government Agencies and their contractors. Other requests for this document shall be referred to controlling office.

☐ **DISTRIBUTION STATEMENT D.** Distribution authorized to the Department of Defense and U.S. DoD contractors only. Other requests shall be referred to controlling office.

☐ **DISTRIBUTION STATEMENT E.** Distribution authorized to DoD Components only. Other requests shall be referred to controlling office.

☐ **DISTRIBUTION STATEMENT F.** Further dissemination only as directed by controlling office or higher DoD authority.

Distribution Statement F is also used when a document does not contain a distribution statement and no distribution statement can be determined.

☐ **DISTRIBUTION STATEMENT X.** Distribution authorized to U.S. Government Agencies and private individuals or enterprises eligible to obtain export-controlled technical data in accordance with DoDD 5230.25.

COPY

ARO FINAL TECHNICAL REPORT

Reporting Period: 1 October 2005 – 30 September 2007

University of California at Berkeley
Principle Investigator: Professor Albert P. Pisano
Project Title: Electro-Magnetic Actuated Valve for MEMS Fuel Metering System

Overview

The goal of this research project is to develop a fuel injection system which delivers the desired ratio of air/fuel mixture to small scale internal combustion engines. Small scale engines require precise fuel control, but the fuel delivery system must be small and low-power. Our research is focused on the development of a planar fuel valve with high fuel delivery rates. The planar nature allows for successful system integration with small scale engines and systems. The fuel valve is electromagnetic, as electrostatic systems are not compatible with liquid fueled systems. The valve design is designed to have a very large open to closed fluidic resistance ratio such that when the system is not being operated, that the fuel delivery rate is near zero (i.e. the valve does not leak).

Milestone Achievements

A. Actuator Design and Analysis

A-1 Finite Element Analysis

A simplified meso-scale electro-magnetic actuator has been designed to determine model boundary parameters and a FEM model has been developed and validated. This model is then used to guide the microscale electromagnetic circuit design.

A micro-scale electro-magnetic actuator has been simulated to determine magnetic flux density, applied current density, magnetic field intensity and forces acting on the actuator. Design of suspensions has been developed to guide an armature, and displacement of the actuator and stress on flexures are simulated.

A-2 Valve Sizing Analysis

A magneto-static actuator has been optimized to maximize force output and to minimize power consumption. Genetic Algorithm (GA) with an interior-penalty method has been implemented to determine the optimal set of geometrical dimensions without violating constraints.

A-3 Process/Mask Design

Process Design

We integrated the electroplating process with the hole-in-the-wall recipes using dry film resist. This process enables an integrated NiFe armature with a hole-in-the-wall within the main flow channel.

20080917037

Mask Design

Four layers of mask for an integrated the valve and the optimized actuator have been designed and fabricated. A set of masks contains three different configurations of gate valve designs, two different fluidic channel width designs.

A-4 Coil/Circuit Design

The actuator test platform to measure the stall force and its flux saturation is designed. The linear stepper actuator for the testing device has 6-teeth and 2phase design with the same critical dimensions of the actuator for the valve system.

B. Fabrication

B-1 Valve Prototype

Recreation and calibration of hole-in-the-wall recipe

The "hole-in-the-wall" valve was recreated with a minor recipe modification according to the change of the valve size. It was successfully formed on a 100μm thick Si device layer on a SOI wafer.

Dry film resist process development

The recipes to use 40 micron thick dry film resist (DuPont FX940) to integrate hole-in-the-wall process and the consecutive electro deposition process were developed and tested.

Electro-deposition

A feasibility of "over-covered" dry film resist has been investigated. The over-covered film has prevented deposition of excessive electro-deposited Nickel Iron over the silicon device layer, and the technique is verified with a series of Scanning Electron Microscope (SEM) image. The over-covered film technique has been implemented the design of the second mask for the optimized actuator.

B-2 Coil/Circuit

The NiFe parts for the actuator test structure are cut from 100 micron and 1mm thick NiFe sheets using wire-EDM and assembled to the wafer.

C. Testing

C-1 Coil/Circuit testing with a dummy motor

The actuator testing platform was fabricated and assembled. The stall force of the actuator test structure was measured. With input of 1A current through 300 turns on the flux guide, the actuator showed 0.97 mN force output.

C-2 Prototype Valve Testing

The MEMS liquid fuel delivery system demonstrates three distinct flow rate regions with respect to the gate positions. Experimental tests were performed to measure mass flow rate, driving pressure and pressure drop across the valve, and two different encapsulation methods have been implemented. The fluidic characterization demonstrates that the system is able to deliver up to 0.5 mg/sec of deionized water with EM actuation and up to 9.5 mg/sec with high driving pressure regions. The maximum fluidic resistance and fluidic resistance ratio of the closed to the open position are determined as 1.83x1015 Ns/m5 and 1.82x102 respectively. The MEMS liquid

fuel delivery system has demonstrated the capability to deliver 428 Watts of chemical energy into the small-scale combustion power system.

Research Summaries

A. Actuator Design/Analysis

A-1 Finite Element Analysis

1.) Meso-Scale Prototype and Determination of Boundary Conditions

A design model has been developed to predict performance of an electro-magnetic actuator. Finite Element Method (FEM) package (cosmosems) has been utilized to simulate the performance of the actuator. On a FEM simulation, the boundary conditions are critical. Therefore, we have developed a meso-scale prototype which has been characterized to provide the experimental validation for the input boundary conditions of the FEM model. This meso-scale prototype is simplified and merely serves to validate the model which will be used to optimize future designs (Figure 1).

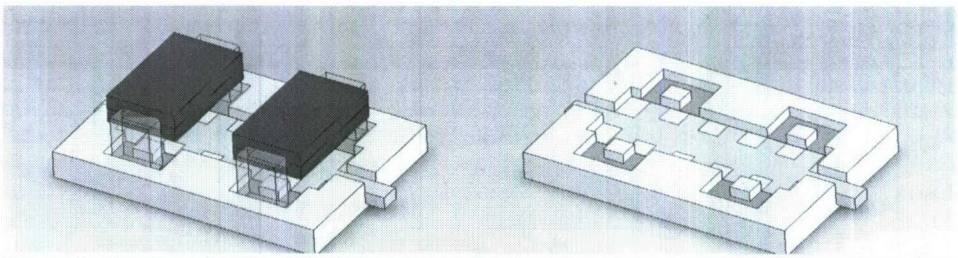

Figure 1: Design of a simplified electro-magnetic actuator to determine proper boundary conditions

The prototype is fabricated with Computerized Numerically Controlled (CNC) machines with mild steel as materials for an armature, flux guides and stators. Overall dimensions of the prototype are designed to be approximately thirty times larger than a proposed MEMS actuator for ease of fabrication and minimal development time (Figure 2). Overall length of an armature is designed as 38.1mm (1.5"), and armature teeth have dimensions of 2.54mm (width) x 2.54mm (height). Air gaps between an armature and flux guides are set as 0.051mm (0.002"). Future testing will examine the impact of fuel filled gaps, which are expected to some degree in practice.

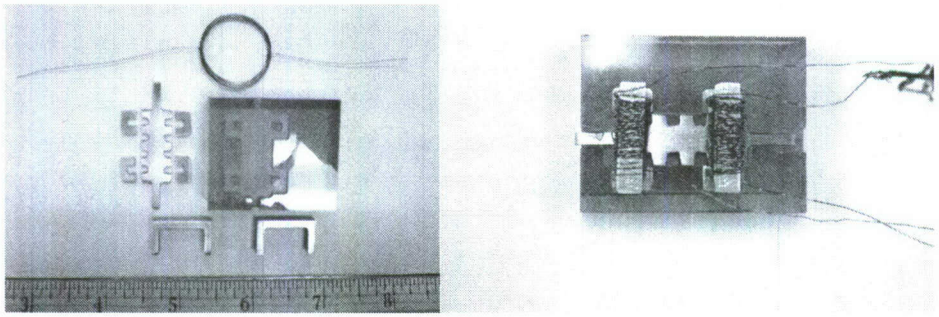

Figure 2: The CNC machined prototype of an MEMS electro-magnetic actuator

In order to actuate this prototype, a commercial D-cell battery has been implemented to induce electric field, and forty turns of 30 AWG copper wire is used (Figure 3.1). During actuation, both the input current and resulting linear force on the armature have been measured with an ampere meter and with a load cell respectively (Figure 3.2). This *unoptimized* prototype actuator produces 21mN of linear force with 2.6A input current to copper wire. The actuation voltage is roughly 1.5V.

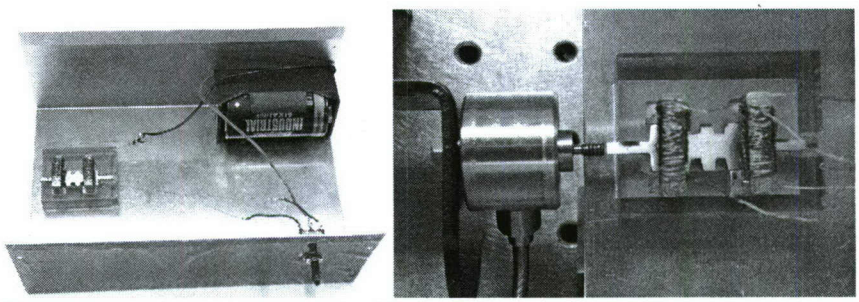

Figure 3: (1) The package of prototype actuator (Left), (2) Linear force measurement apparatus (Right)

The FEM model is examined for grid sensitivity by varying outside air volume and grid size of air gaps. Outside air volume determines the effective volume of electric and magnetic field while the size of air gap grid determines accuracy of the prediction. Experimental measurements are implemented as inputs of the simulations. Input parameters such as input current and number of wire turns are kept same values as experiments. With same input current (2.6A), and same turns (40 turns) of wire, the FEM model is carried out to determine the predicted linear force exerted on an armature. Boundary conditions, such as outside air volume, of each simulation are varied, and a resulted linear force is compared with an experimental result. The purpose of these simulations is to provide accurate boundary conditions for MEMS actuator simulations with the minimum computation time.

As noted above, a parametric study (or sensitivity analysis) of the surrounding air volume and grid spacing was carried out. Different outside air volumes and size of grids for air gaps between an armature and flux guides, and air gaps between armature teeth are implemented to determine correct approximation of the air gaps between the armature and flux guides with minimum computation time. Air volume has been reduced from 15 times of the prototype volume ($340cm^3$) to 1.5 times of its volume ($37.7cm^3$). Since it is required to have longer computation time for bigger outside air volume, these sets of simulation provide the minimum computation time and the minimum computation tool system requirements without sacrificing accuracy of the prediction (Table 1).

Air Volume (cm^3)	37.7	127	340
Linear Force (mN)	16.1	14.6	14.6

Table 1: Variation of a resulted linear force according to outside air volume

It should be noted that all these simulation utilized same grid size as followings (Table 2).

	Base	Armature	Flux	Bridge	Coil	Air	Air	Air

			Guides			gap1	gap2	gap 3
Grid Size (mm)	2.5	2.1	1	2.1	2.11	0.1	0.5	0.37

Table 2: Common grid size for determining outside air volume

Note: Air gap1: air gap between armature and flux guides; Air gap2: An armature teeth air gap; Air gap3: air gap between an armature and base

The result of these simulations show that the prediction of linear force, which exerted on an armature, does not vary until the air volume is reduced to up to 1.5 times of the prototype volume. This reduced amount of air volume can be directly implemented to rest of simulations to reduce computation time.

Air gap grid size has been reduced from 0.15mm to 0.05mm. The prediction determines that the results are the most sensitive to these gaps. With air gap grid size as 0.05mm, which provides one grid between the armature and flux guides at the smallest gap locations, and outside air volume as 1.5 times of actuator volume, the simulation predicts 22.5mN of actuation force exerted on an armature (Table 3).

Air Gap Grid Size (mm)	0.15	0.1	0.05
Linear Force (mN)	11.6	16.1	22.5

Table 3: Variation of a resulted linear force according to air gap grid size, 37.7cm3 total computation volume

This prediction is close to experimental result (21mN) with 7% prediction error. This initial result shows that relatively accurate predictions can be estimated with minimum of one grid for the smallest air gap with minimum air volume as two times larger than the actuator.

As results of the prediction, magnetic flux density, magnetic flux intensity, applied current density and linear force for each axis are obtained (Figure 4). The error in the model is attributed to the unevenness of copper wiring on the prototype bridge. The prototype coils were wound (40 turns) manually leading to non-uniform flux distribution. This error is expected to be reduced by using commercially available winding coils. Despite this small offset of linear force, the validity of the model has been achieved and the model will be applied to the initial designs of the micro-scale actuator. As this prototype and simulation are for the meso-scale device, these results will suffice for the time being and these simulations will be used to assist the experimental design by assisting in the parameter selection for the parametric design.

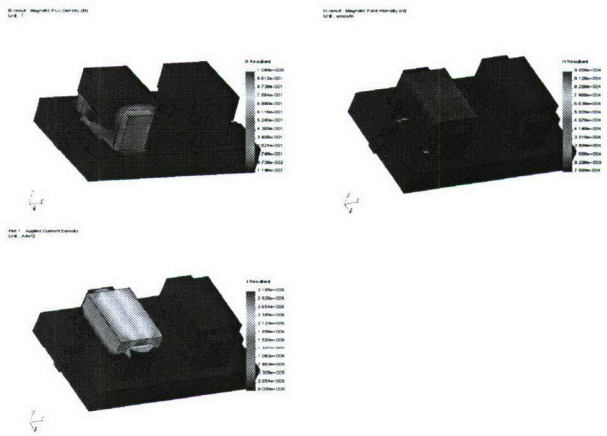

Figure 4: The results of FEM simulation for prediction of force fields for the prototype actuator

2.) Design of micro-scale actuator and simulation of electro-magnetic forces

A design model for a micro-scale electro-magnetic actuator has been developed. A simplified model of micro-scale actuator has been built with a CAD tool (Solidworks), and simulated with a FEM package (Cosmosems). This simplified actuator model does not include suspension design for guiding an armature movement, and has four phases as a proposed design (Figure 5). This model is utilized material properties of Silicon (Si), Copper (Cu), Nickel Iron (NiFe), and air.

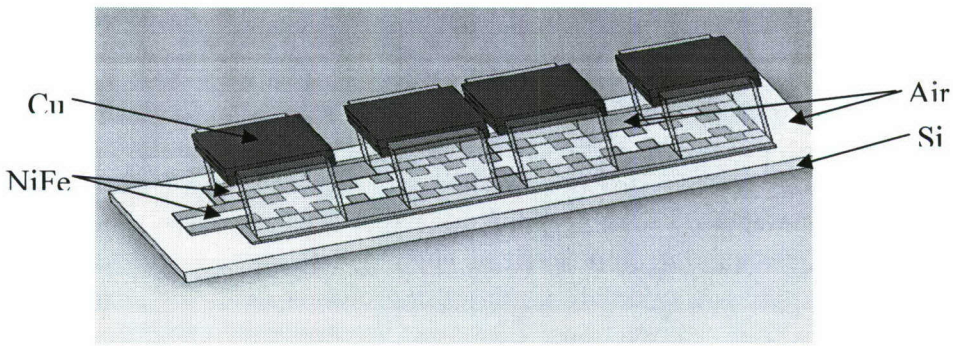

Figure 5: Design of a simplified a micro-scale electro-magnetic actuator

In order to simulate a semi-conducting ferromagnetic actuator, electro-magnetic properties of Si, air, Cu and NiFe are defined and shown table 4. It is assumed that the properties of materials are independent of orientation (i.e. isotropic materials).

	Relative Permeability	Conductivity (S/m)
Si	1	0
Air	1	0
Cu	0.99991	$5.7X10^7$
NiFe	2000	$5X10^6$

Table 4: Electro-magnetic properties of a micro-scale device simulation

From knowledge gained in the previous section, critical boundary conditions (air gap grid size and outside air volume) have been set as one grid for the smallest air gap between an armature and flux guides, and 1.5 times of actuator volume respectively. Input current of 0.06A with 1000 turns of wire (NI = 60) is set as a default input parameter.

As results of a simulation, magnetic flux density (B), applied current density (J) and magnetic field intensity (H) and linear force exerted on armature in three directions are obtained (Figure 6). Force directions in an armature moving direction, gap closing direction and out of plane direction are denoted as subscription of x, y and z.

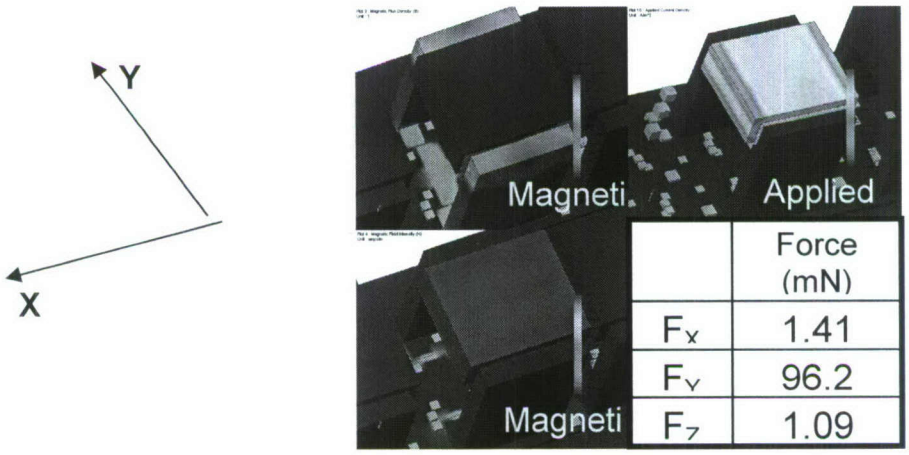

	Force (mN)
F_x	1.41
F_y	96.2
F_z	1.09

Figure 6: The results of FEM simulation for prediction of force fields for the micro-scale electro-magnetic actuator

The results of the simulation indicated that the force in gap closing direction is significantly larger (70x) than the force exerted in the armature moving direction. With consideration of desired armature displacements (200μm for an armature moving direction and less than15μm for a gap closing direction), spring constants for the guiding suspensions are determined as 7 N/m for the armature moving direction and 6000 N/m for the gap closing direction. This result implicates the design of suspension requires to be 860 times stiffer in the gap closing direction than the armature moving direction. This high ratio of stiffness in directions suggests a folded suspension design.

3.) Design of folded suspensions and simulation

In order to accommodate the high ratio of stiffness between a gap closing direction and the armature moving direction, a design of four folded suspensions is adapted for this application (Figure 7). A MATLAB code has been developed to determine lengths of suspension to achieve desired stiffness in both directions. This code determines spring constants and bending stresses while varying lengths of two long beams (L2 and L3). The thickness of the suspension is constrained by thickness of an armature (100μm) as determined by fabrication methodology and the width of beam is an additional parameter to be optimized. The beam width is currently set by a realistic fabrication tolerance (aspect ratio) optimized for high process yield. These computed spring constants and stresses are compared with its given values of stiffness, which are

determined from electro-magnetic force simulation, and with yield stress of Si. The code displays satisfied pairs of L2 and L3 as outputs. This suspension design includes a big anchor, which is located 10μm apart from an armature, to provide additional stiffness in a gap closing direction and to serve as an armature guide to prevent in plane rotation. In addition, the large anchor prevents deformation of armature due to high gap closing bending force

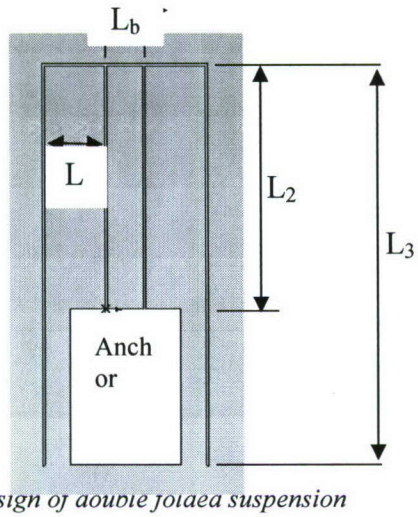

Figure 7: The design of double folded suspension

A FEM simulation is performed to determine width of beams and optimum length of L2 and L3, which are determined from a MATLAB code. Four double folded flexures are adapted on this simulation (Figure 8). Boundary condition of anchors is set as fixed and predicted linear forces from an electro-magnetic simulation are implemented as input forces. Outputs of this simulation are overall displacement, stress, and factor of safety.

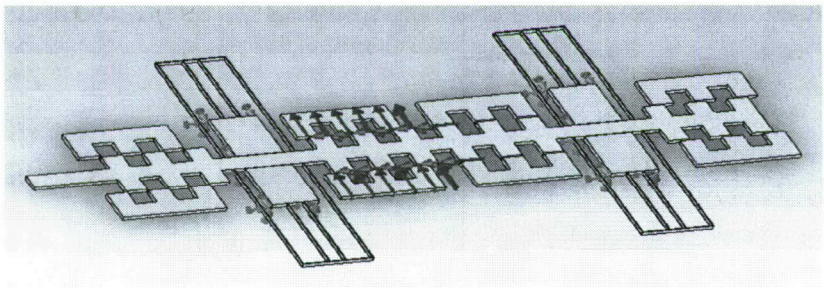

Figure 8: Boundary conditions and exerted forces acting on a micro-scale electro-magnetic actuator

The width of the beams has been parametrically varied to determine how the armature displacement and stress of the suspensions are affected. With 15μm beam width, the simulation produces 190μm of armature displacement (Figure 9a). In addition, a large anchor, which is located 10μm from the armature, suppresses armature movement in a gap closing direction, and

prevents contact between an armature and flux guides. Overall the parametrically optimized dimensions of the suspension for this simulation are given in table 5. It is noted that the distance between sidewall of anchor and beam L3 is 210μm, and beam L3 will not have contact with anchor when the armature has maximum displacement.

	L1	L2	L3	Lb	Width	Thickness
Length (μm)	500	2000	3305	328	15	100

Table 5: Calculated dimensions for double folded suspension

A stress analysis is subsequently performed on corresponding dimensions of the suspension. The maximum stress within the structure for this design is determined to be 106MPa, which is five times less than silicon yield stress (Figure 9b). The minimum safety factor of the suspension design is therefore determined to be 4.7 (Figure 9c) which should prevent any brittle fracture due to applied stress. The results of a FEM simulation verifies that the design of suspension provides robust and high endure suspension for the actuator.

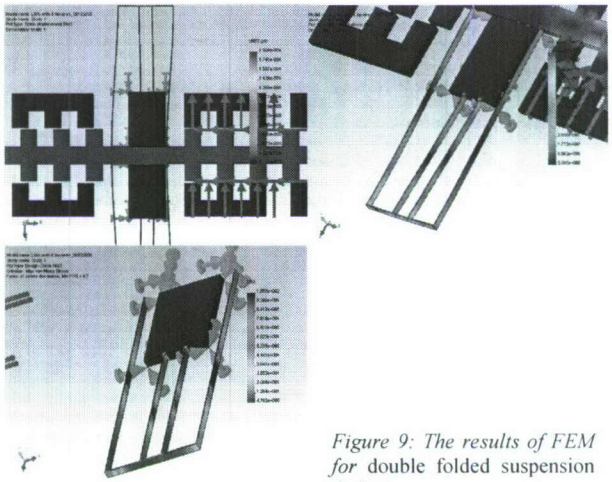

Figure 9: The results of FEM for double folded suspension design

A-2 Valve Sizing Analysis

Design Optimization of a MEMS Magneto-Static Linear Actuator

Optimization Problem

Current design of a MEMS magneto-static actuator was simulated to produce 1mN actuation force, but it is not optimized for minimizing required power and/or maximizing force output by the actuator. In addition, it is not optimized for maximizing throughputs (minimizing die area per actuator). Design optimization, therefore, has been performed with an optimization tool (Genetic Algorithm) with an internal penalty method. Objective function has been setup as minimizing the die area, and other objectives (minimum power requirement and maximum force output) are represented as constraints, ensuring the minimum performance criteria for the device.

Objective Function

Given that the ultimate goal of this optimal design problem is to minimize the die area of the device, the objective function that is posed is the standard:

(1) $A = L_s W_s$

Where L_s is the length of one stator, W_s is the total width of the stator

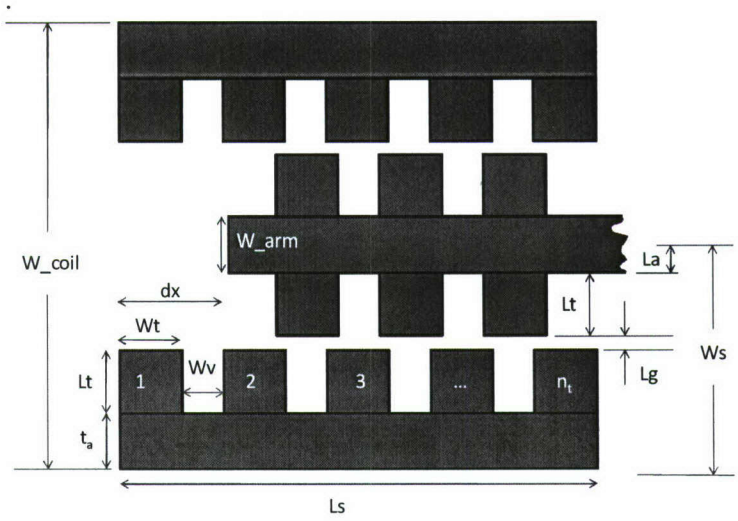

Figure 10: Actuator geometry showing both design variables and parameters

Figure 10 shows all the relevant design variables and parameters. While the optimization function appears elementary, the constraints needed for proper device function yield a more complex problem.

Inequality Constraints

The problem has the following inequality constraints:

(2) $F \geq F_t$

(3) $I \leq I_{max}$

(4) $L_g \leq 10h$

(5) $L_s \geq L_{s,min}$

(6) $L_s \leq L_{s,max}$

(7) $L_t, L_g, W_v, W_t, t_a \geq L_{res}$

(8) $t_a \geq t_{a,min}$

(9) $n_t \geq 1$

(10) $0.4W_t \geq \delta$

(11) $N \leq N_{max}$

The actuator force inequality listed in equation (2) is of primary importance as it will govern whether or not the valve can adequately meter the flow in the fuel channel. The electric current (i) limitations will be set by whichever power source is utilized for the device (battery, DC source, etc.) is also restricted as most MEMS devices have small power limitations. The overall stator dimensions as listed in equations (4) through (8) confine the stator into a finite box that both accounts for manufacturing tolerances on the lower end and geometry interferences with other device components. And lastly, for equation (11), N is the number of coil turns allowable in the magneto-static actuator is based on the stator coil bridge length.

Equality Constraints

The following equality constraints manifest themselves through the physical derivation of the formulas which govern the response of the device. The first constraint comes from an electro and magnetic actuator design handbook which states that the width of the stator teeth are equal in length to the valley width.

(12) $\frac{W_t}{W_v} = \phi = 1$

Additionally, the tooth height (L_t), is a ratio of the teeth pitch:

(13) $L_t = 0.4(W_v + W_t)$

Where *Wv* and *Wt* are the valley width and the tooth width respectively.

The number of coils is determined by 2x the overall width of the stator width and the diameter of the coil. This number of coils however can be multiplied by integer factors due to the number of coil overlaps one could generate:

(14) $N = \frac{2W_s}{D_{coil}}$

Adding further to the confined geometry of magneto-static actuator designs, the ratio of the teeth thickness, the valley width to the gap distance is defined to be a parameter T_p , which defines a specific set of numerical constants to be used in the linear force equation.

(15) $T_p = \frac{(W_v + W_t)}{L_g}$

The length of the stator, which is one of the variables in the objective function, is calculated as follows:

(16) $L_s = n_t W_t + (n_t - 1)W_v$

Where n_t is the number of teeth present in the design. Equation (17) demonstrates how the mass is calculated.

(17) $m = \rho h\left(n_t L_t W_t + L_a W_v(2n_t - 1)\right)$

And finally, W_s, the width of the stator is a function of half the armature width (La), the length of the teeth, the gap distance, and the anchor thickness, *ta*.

(18) $W_s = L_a + 2L_t + L_g + t_a$

The literature suggests T_p values of 20, 30, 40, and 50 and optimization analyses will be performed on each case [2]. However, since part of the original optimization problem was to maximize force, a quick review of the design tables presented in [1], [2] allows one to find the maximum constants residing with T_p equal to 50. This allows for the simplification of the force function for the optimization problem and also relieves the headache of coding in standardized, empirical tables.

One of the most important equality equations in this analysis—the actuation force—is presented below in equation (19) and derived in the following section: **Error! Reference source not found.**.

(19) $f = \frac{1}{8}N^2 n_t^2 i^2 \mu_o h[C_1 \sin n_t x + 2C_2 \sin 2n_t x + \cdots]$

Simplifying the above force equation by reasoning that the force will be max when the $\sin(90^o) = 1$ and by dropping the rest of the approximating terms and constants (C_2-C_n):

(20) $$f = \frac{N^2 n_t^2 i^2 \mu_0 h C_1}{8(W_s - t_a)}$$

By allowing T_p to be set to 50, this allows us to drop the sine terms and approximate f as a linear function with respect to C_1.

Design Variables and Design Parameters

With all of the aforementioned equality and inequality constraints, many were represented in terms of design variables and design parameters. This optimization problem has the following Design Variables and Design Parameters:

Table 6: List of Design Variables and Design Parameters

Design Variables		Variable Definition	
1	i	Current	Amps
2	N	Number of Coil Turns	-
3	n_t	Number of teeth	-
4	W_s	Stator Width	μm
5	L_s	Length of the stator	μm
6	W_v	Valley width	μm
7	W_t	Width of stator teeth	μm
8	L_g	Gap distance	μm
9	f	Force	N
10	L_t	Tooth Length	μm
11	t_a	Anchor Length	μm
12	m	Mass	Kg

Table 7: List of Design Parameters

Design Parameters				Units
1	D_{coil}	=	0.2	mm
2	$L_{s,min}$	=	2	mm
3	F_t	=	3	mN
4	Tp	=	50	-
5	h	=	100	μm
6	i_{max}	=	100	mA
7	N_{max}	=	500	turns

8	μ_o	=	$4\pi \times 10^{-7}$	Henry/m
9	L_{res}	=	2	μm
10	Wv/Wt	=	1	-
11	C_1	=	8.3	-
12	m_{max}	=	1.83×10^{-6}	Kg
13	ρ	=	8770	Kg/m^3

Analysis

Derivation of Linear Force Equation

Linear force of a magneto-static actuator is approximated as the following.

(21) $$F = \frac{\partial W}{\partial x} = \frac{1}{2}\frac{\partial L}{\partial x} i^2$$

Where L is the self inductance and i is the input current. The self inductance can be approximated as $L = N^2 P$ where N is number of coil turns and P is the permeance [Weber per ampere-turns]. Linear actuation force, therefore, becomes a function of $\frac{\partial P}{\partial x}$, and it can be shown as the following:

(22) $$F = \frac{1}{2} N^2 i^2 \frac{\partial P}{\partial x}$$

The permeance, P, as a function of an armature location, x, is therefore:

(23) $$\sum P(x) = \frac{1}{4} n_t \mu_o h[C_1 \sin n_t x + 2C_2 \sin 2n_t x + \cdots]$$

Expressions (22) and (23) give the linear force as a function of distance, x:

(24) $$F = -\frac{1}{8} N^2 n_t^2 i^2 \mu_o h[C_1 \sin n_t x + 2C_2 \sin 2n_t x + \cdots]$$

Where N is the total number of coil turns in the phase. To simplify this function further, as discussed earlier, one achieves:

(25) $$f = \frac{N^2 n_t^2 i^2 \mu_0 h C_1}{8(W_s - t_a)}$$

The division of $W_s - t_a$ is explained by the fact that the force function is derived from a rotary magnetostatic actuator. Thus, to convert this torque into a force, the equation needs to be divided by a fictitious moment arm which is approximated by the overall width of the stator minus the thickness of the anchor.

Derivation of minimum force requirement (F_t)

One of the main constraints present in this design optimization is the force achievable by the magneto-static actuators. In order for successful device operation, it is crucial that a critical threshold force is achieved to effectively meter the fuel delivery to the combustion chamber. This F_t can be determined to first order by applying a linear momentum balance to a control volume specific to this application. This method can be found in any elementary text in fluid mechanics.

Before a rigorous analysis is performed, some assumptions were made to simplify the problem were utilized (seen in Table 3).

Table 8: Tools and assumptions used in the problem formation

Tools Used	Assumptions Made
▪ **Linear**	▪ **A single channel protrusion can**

Momentum Balance for Fluids ▪ **Control-volume analyses**		**be modeled as two symmetric protrusions** ▪ **The flow in the channel is *incompressible*** ▪ **Viscous forces and effects are neglected** ▪ **The pressure after the protrusion(s) is at vacuum ($P_2 = 0$)**

The following figures illustrate the problem formation and the associated control volume used with forces, flows, and the like labeled for clarity.

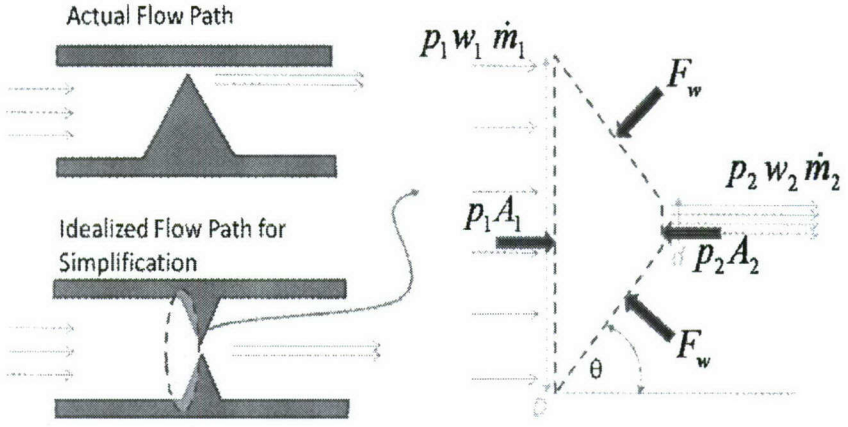

Figure 11: (Left) Assumption used to simply flow problem. (Right) Control volume used to calculate force on actuating valve

The following problem parameters are defined in the following table:

Table 9: Definition of parameters

Parameter	Definition
$\dot{m}$	Mass flow rate either entering (1) or exiting (2) control surface [kg/m^3]. For the small-scale rotary engine, the mass flow rate is approximately 40mg/cm^3
p	Pressure at either the inlet or outlet of the control surface [Pa]. P_1 is the fuel pump pressure which is approximated at 1.5 atm. P_2 is assumed to be at vacuum and thus is at 0 psi.
w	Flow velocity at the inlet or outlet of a control surface [m/s]
F_w	Force "felt" on the front surface of the valve [N]
θ	Angle of the valve plunger surface [radians]
ρ	Density of the fluid flowing through the channel.

$$\rho_{CH_3OH} = 792\,kg/m^3$$

The linear momentum problem starts with the following equation:

(26) $$\frac{\partial}{\partial t}\int_{CV} w\rho dV + \int_{CS} w\rho\vec{\boldsymbol{V}}\cdot\hat{n}dA = \sum F_x$$

(27) $$0 + \int_{CS} w_1\rho(-w_1)dA_1 + \int_{CS} w_2\rho(+w_2)dA_2 = p_1A_1 - p_2A_2 - 2F_{w,x}$$

Where the system is at steady state making the transient change of the momentum, zero. Additionally, $F_{w,x}$ is simply the component of the wall resistance force in the *x-direction*. The force in the *y-direction* can be calculated from knowledge of $F_{w,x}$. Positive x is defined going from left to right. Further reduction and solving for $F_{w,x}$ yields:

(28) $$F_{w,x} = \frac{1}{2}\left(p_1A_1 - p_2A_2 + \dot{m}(w_1 - w_2)\right)$$

Where the mass flow rate is the same for the inlet and outlet and thus $\dot{m}$ could be substituted for $\dot{m}_1$ and $\dot{m}_2$. Plugging in known values and solving for the various parameters, the force was calculated:

(29) $$F_{w,x} = 0.0025N \Rightarrow \frac{F_{w,x}}{\sin\theta} \Rightarrow F = 0.0025N$$

(30) $$F_{w,x} = 0.0025N \Rightarrow \frac{F_{w,x}}{\cos\theta} \Rightarrow F = 0.0029N$$

(31) $$F_{w,y} = \frac{F_w}{\sin\theta} = 0.0015N = 1.5mN$$

This value for $F_{w,y}$ is conservative and correlates with fluid-flow simulations which had $F_{w,y} \approx 1.3mN$. Thus, the threshold force is equal to $F_{w,y}$ provided no factors of safety (FOS) are applied. Using a FOS of 2, the threshold force is equal to:

(32) $$\boxed{F_{y,threshold} = 3mN}$$

Optimization Formulation

Genetic Algorithms

Genetic algorithm (GA) has been adapted for the optimization because it works in parallel on a population of individuals, and thus can ensure a better exploration of the design variable space. A MATLAB genetic algorithm toolbox is utilized for optimization, and the GA toolbox is based on the augmented lagrangian genetic algorithm.

Initial attempts of minimizing an objective function with separated equality constraints and inequality constraints was confronted and presented difficulties in finding feasible points via the genetic algorithm program, and the program terminated. Probability of randomly generated individuals located out of bounds increases exponentially as constraints are increased, and hinders the solution convergence of the program.

Therefore, a penalty method has been implemented to the optimization process to convert constrained problem into unconstrained problem. All equality constraints (Eqn. (12) through

(15)) are solved for one design variable (lg) and substituted into the objective function, and three inequality constraints are normalized and placed as barrier functions.

Barrier function (Interior-point penalty function) has been adapted to the objective function because boundary of variables is known, and feasibility is preserved at all times. Logarithmic barrier functions are added and the objective function transformed into a pseudo-objective function.

$$T(x) = y(x) + \frac{1}{r_k} B(x) \quad (33)$$

where y(x) is the objective function, r_k is a penalty parameter, and B(x) is a barrier function. This logarithmic barrier function has been adapted into the objective function of the magneto-static problem and produced the following equation.

$$T(x) = y(x) + \frac{1}{r_k} \sum_{i=1}^{3} \ln(-g_i(x)) \quad (34)$$

Where r_k is weight of penalty function and g(x) is inequality constraint. Therefore, the pseudo-objective function with barrier functions becomes the following.

$$T(x) = y(x) + \frac{1}{r}(\ln(-g_1) + \ln(-g_2) + \ln(-g_3)) \quad (35)$$

Where $y = (t_a + 2l_t + l_g + l_a) * (n_t * w_t + (n_t - 1) * w_v)$

Minimum force inequality constraint

$$g_1 = 1 - \frac{1000 * (N * n_t * i)^2 \mu_0 h C_s}{F_{min} * 8 * \left(\frac{L_s}{2\Pi} + l_t + l_g\right)} \quad (36)$$

Maximum mass inequality constraint

$$g_2 = \frac{\rho * h * (n_t * l_t * w_t + l_t * l_s)}{Mass_{min}} - 1 \quad (37)$$

Minimum stator length constraint

$$g_3 = l_s = 1 - \frac{n_t * w_t + (n_t - 1) * w_v}{l_{min}} \quad (38)$$

Penalty parameter (r_k) has been increased an order of ten for each iteration, and the process is terminated when no improvement in the pseudo-objective function is achieved as increase of penalty parameter and all constraints are satisfied.

Boundaries for four design variables are constructed (Table 10). Anchor width (t_a) is bounded by required minimum length for a stator in that it needs to provide space for the coil bridge foot. Conversely, the maximum length is constrained due to the magnetic flux leakage, which becomes significant at larger values. Length of teeth (l_t) is bounded for minimum safe fabrication limit and allowed maximum magnetic flux density before saturation. Number of

teeth on the stator is bounded by minimum of linear-force generation, and by allowed maximum magnetic flux density.

Table 10: Bounds for the numerical optimization algorithm

Lower Bound	Design variable	Upper bound
2mm	Ta	4mm
0.02mm	Lg	0.05mm
2 [-]	nt	5 [-]

Four sub-vectors of Population size 100 are created to compute, 500 generations (iterations) are allowed to find a converged solution set.

Results

Genetic Algorithms

Genetic algorithm generates potential optimum values for the objective function, and the optimum values are shown on Table 11.

The pseudo-objective function converges as penalty parameter (r) increases (Figure 12). It is noted that some values of the objective functions became an imaginary number because not all of constraints are satisfied. However, with penalty parameter (r) becoming greater than 10^5 the optimum values are satisfied constraints (force, mass and stator length), and the function converges into a single value.

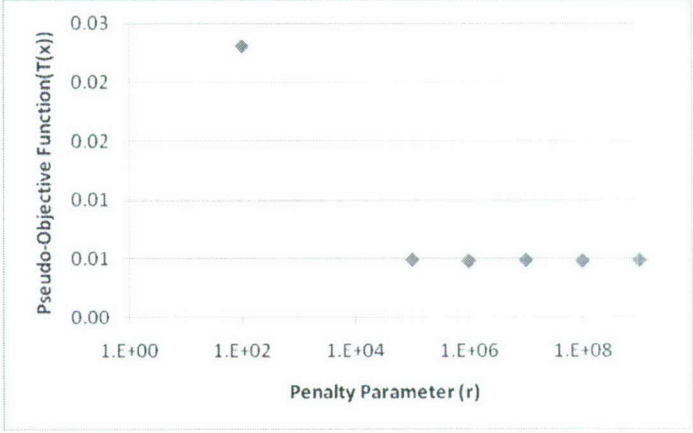

Figure 12: Plot showing convergence of genetic algorithm

From the GA simulation, the optimum design variables are determined as the following (Table 11). It is noted that the converged optimum values are either located at lower boundary (lg) or upper boundary (*ta* and *nt*).

Table 11: Optimal set of values as found from the genetic algorithm

Ta [mm]	*Lt [mm]*	*Lg [mm]*	*Nt [-]*	*Force [mN]*	*Mass [mg]*	*Stator length*	*Area mm2*
3.96	0.4	0.02	5	7. 16	1.84	4.43	20.5

Using the optimum set derived from GA, the optimal set of design variables can be implemented into a 3D CAD program and modeled to observe the differences between current design and optimized design. SolidWorks™ 2007 was used to model the optimized flux guides (Figure 13).

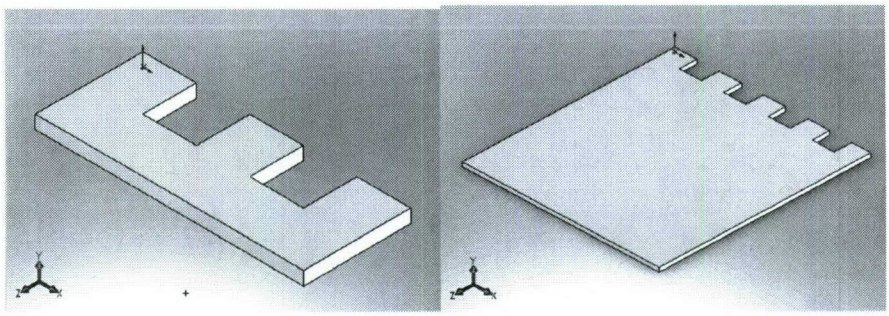

Figure 13: (Left) Stator geometry as originally designed (Right) Optimized stator geometry

The optimal actuator is shown below in the following Figure14.

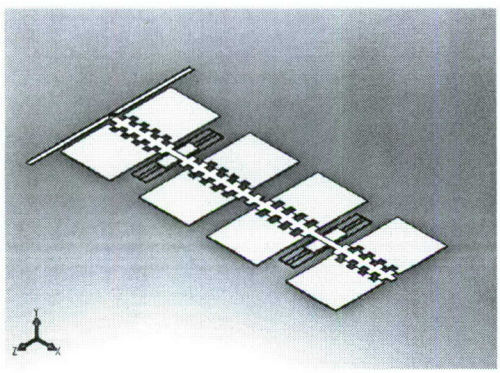

Figure 14: Geometrically optimized linear magneto-static actuator (with respect to stator area)

A-3 Process/Mask Design

Process Design

One fabrication task was to develop a dry film resist process to be used in conjunction with the hole in wall valve process. We came up with new fabrication process using dry film resist (Figure15). The development of a dry film resist process would make it possible to pattern, etch and electroplate NiFe structures after finishing the hole-in-the-wall process covering large and deep Si structures such as the valve head, the fuel channel, the armature chamber, and armature suspensions on the wafer. This would require minimum modification to the hole-in-the-wall recipes and reduces complication of the integrated process.

The product we tested is DuPont Riston Special FX900 Series. The resist thickness we tested are 15μm, which is the thinnest available in the market, 30μm and 40 μm. The resolution is considered to be approximately the half of the resist thickness. We used an office laminator to control the temperature, speed and pressure of lamination step. Then the resist was exposed by UV light using KS Aligner.

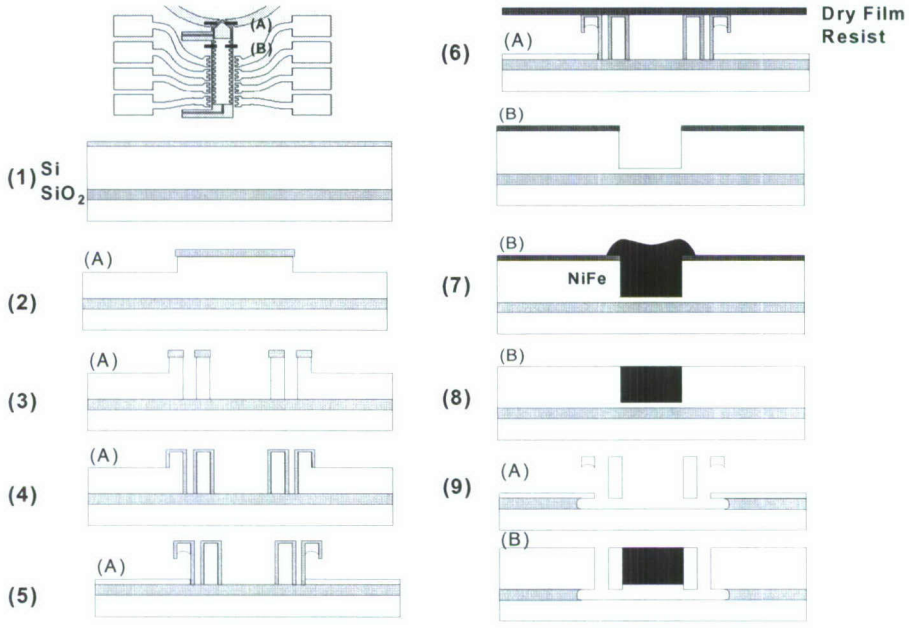

Figure15: Fabrication process using dry film resist

Mask Design

Three layers of the optimized actuator mask have been designed, and. First mask is designed for etching of a silicon device layer, which defines suspensions and moulds for electroplated Nickel Iron. Second mask is designed for electroplating process, which opens only an armature and stators for ferromagnetic metal deposition, and covers rest of the actuator. Third mask is designed for backside etching which helps to release an armature after electroplating process.

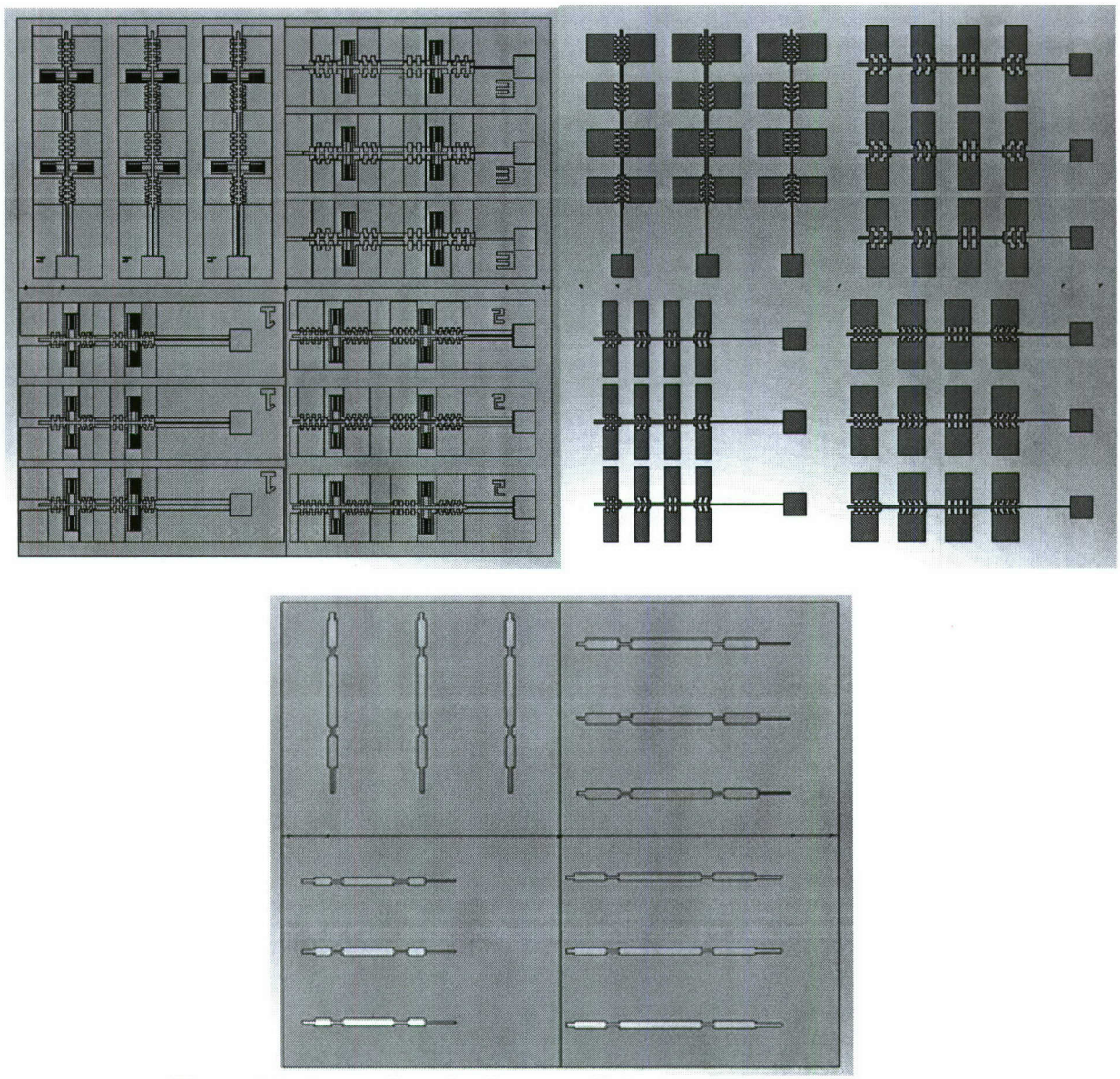

Figure 16: A set of masks for an optimized magneto-static actuator

First mask (Figure 16, Left) contains four different geometrical configurations. Bottom left corner, which is numbered as "1", is denoted for current actuator design configuration, and bottom right corner, which is identified as "2", is designated for the optimized dimensions from the genetic algorithm simulation. Upper right corner, which is numbered as "3", is designed for increased teeth width to 500μm by replacing the current design width of 400μm. At last, upper left corner, which identified as "4", is denoted for reduced air gap distance from 20μm to 10μm.

Second mask (Figure 16 Right) is designed for electroplating process, and produces patterns of 15μm recessed inside from the first mask generated patterns (gray walls) (Figure 17). Second mask is an emulsion mask, which is designed for negative film resist, and it generates patterns that unexposed areas of the mask (orange color) are developed and dissolved. Therefore, the undeveloped film resist (gray color) covers over the silicon vertical wall patterns. The coverage of side walls helps to prevent growth of side-bumps during electro-deposition

process by hiding sidewalls (Figure 18). More details on the technique will be explained on electroplating process section.

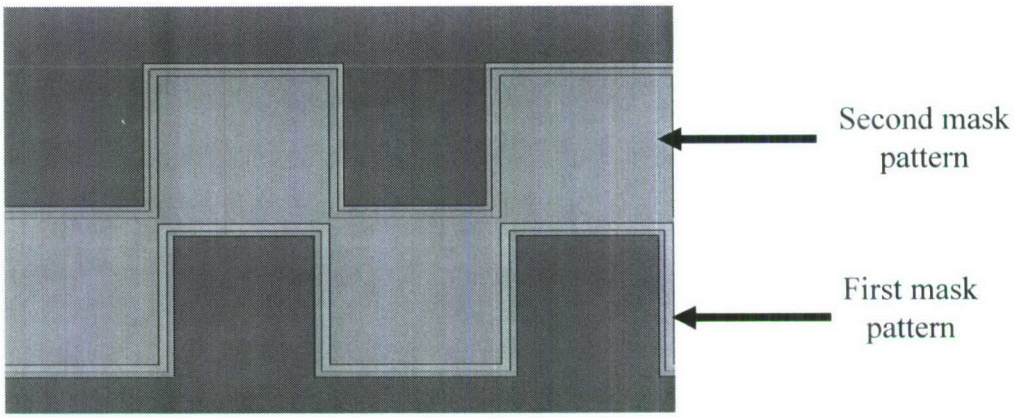

Figure 17: Recessed second mask design

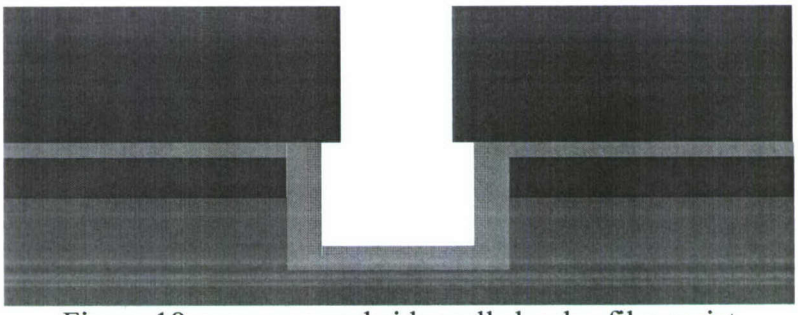
Figure 18: over-covered side walls by dry film resist

Third mask (Figure 18, Bottom) is designed to help release of an armature by backside silicon etching. The mask is used to open oxide of a SOI wafer by etching backside of the device layer, and the exposed oxide layer is attacked by hydrofluoric acid (HF) during final releasing wet etching process. The mask is designed to only etch area underneath an armature to prevent any excessive etching of anchors for folded suspensions. Reactivity, however, between electroplated NiFe and HF is unknown, and has been investigated.

Prior to design the third mask, reactivity of electroplated Nickel iron (NiFe) with HF has been investigated, and determined that there is no reactivity or insignificant reaction rate exists. Continuous eighteen hours of reactivity test between NiFe and HF have demonstrated that insignificant reduction of NiFe has been observed while all deposited oxide is completely removed.

A-4 Coil/Circuit Design

The mask for the testing platform is designed. The purpose of this test structure is to measure the stall force and it's saturation of the linear stepper actuator with the same critical dimensions of the actuator for our valve system.

Figure 19 shows the design of the linear stepper actuator for the test structure.

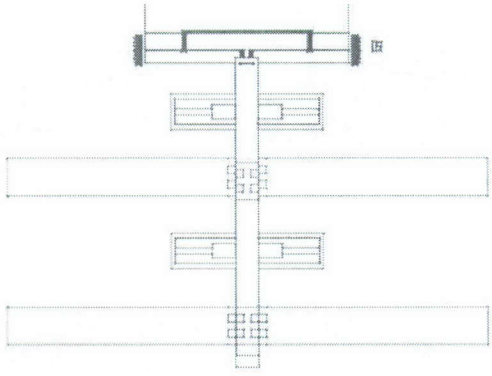

Figure19. Stepper Motor Design

The actuator has 6-teeth 2-phase design instead of 4-phase for actual valve system (Figure20). It still holds same critical dimensions, such as 400μ teeth width, 40μ stator-motor spacing and 15micron suspension beam width. The size of the connecting pad of the magnetic flux guide is 5mm x 5mm.

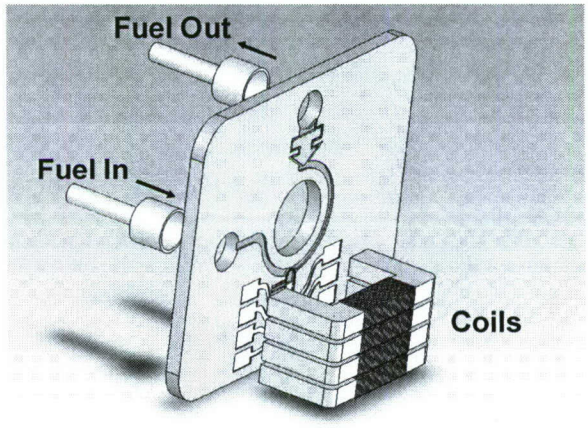

Figure20. Four-phase design valve system

Measurement of the stall force

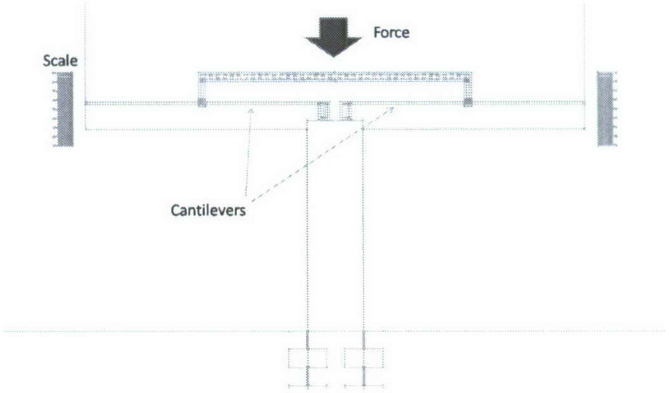

Figure21. Test structure to measure the stall force

This test structure measures the stall force by measuring the bent of cantilevers. We will apply force against the actuator by simply poking the bar and set the Phase (A) at 90 ° while keeping Phase (A) on (Figure 21). The force held by the suspension for the actuator will be compensated.

Measurement of force saturation

The stall fall is approximately;

$$F \approx \frac{1}{8} n_t \frac{2\pi}{\Delta x} N^2 i^2 \mu_0 h c_1 \qquad (39)$$

n_t: Number of teeth
N: Number of coil turns
I: Current applied to coil
h: Height of a tooth
c_1: Factor of teeth/spacing aspect ratio

Note that ferromagnetic materials have a maximum level of flux density B that can be easily carried and this level is called saturation level.

The flux density is described as;

$$B = \mu H = \frac{\mu N i}{l} \qquad (40)$$

The stall force will saturate once the flux density reaches its saturation level with increase of input current. Therefore this saturation level often defines the maximum force that an actuator can create.
We will measure the saturation point of the stall force by simply increasing the input current to the coil.

D. Fabrication

B-1 Valve Prototype

Recreation and calibration of hole-in-the-wall recipe

As a first step of fabrication efforts, we recreate the hole-in-the-wall valve (Figure 22). The original recipe was developed approximately 2years before starting this project using equipments in UC Berkeley Microlab. First, the recipe was tested with original masks on test-grade silicon wafers. After making a few process modifications to accommodate for multi-user tool variability, such as STS DRIE recipe and isotropic etching time, we successfully fabricated hole-in-the-wall structure.

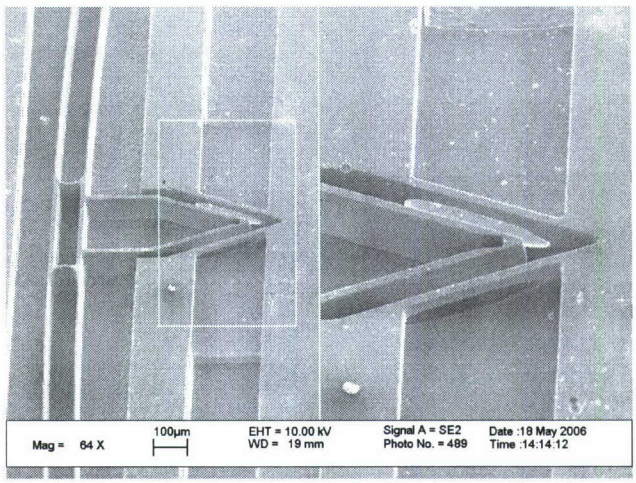

Figure 22: Fabricated hole-in-the-wall valve

Due to changes of dimensions of the valve, we adopted and calibrated a new recipe for the isotropic etch to make a "hole-in-the-wall".

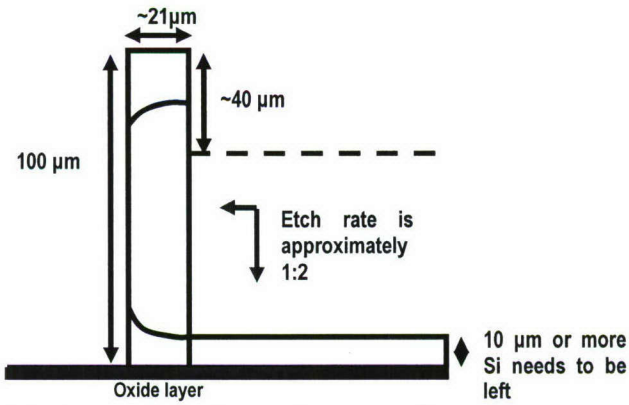

Figure 23: Isotropic etch requirements for our prototype device

The original isotropic etch recipe was developed to make a hole on approximately 16µm thick Si walls (20µm before "undercut" wet etch) laid in 40 degrees across a 200 µm wide channel. Our prototype device has a channel twice as wide, 400 µm, and consequently the wall thickness was changed to approximately 21 µm (25 µm before "undercut" wet etch). The thickness of SOI device layer is kept same as 100 µm (Figure 23).

The challenge is that the etch rate of STS isotropic etch is approximately twice as fast in the

vertical direction as in the lateral direction. In order to maintain certain thickness (10~20μm) of a Si floor as sealing for oxide undercut (~25 μm), which will be made by the release-etch later, the lateral etch can be only done for 25~30 μm range to break a "hole-in-the-wall".

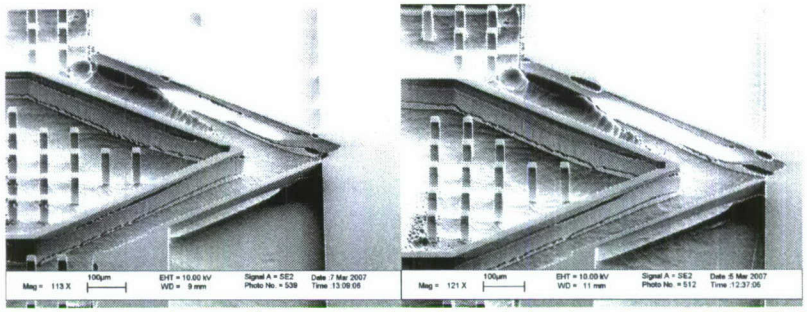

Figure 24: (LEFT) "hole-in-the-wall" made with the original recipe (RIGHT) Hole in the wall made with increased pressure

We found two problems with the original recipe (shown in the LEFT photo of Figure 24). The first is that it does not break a hole all the way through 21μm wall leaving a pole across the hole. The second is that the angled corner of the walls did not get etched well. This seems to be caused by the deprived etchant around the sharp corner we have for 60 degree valve heads.

We tried a new isotropic etch recipe with increased pressure in the STS chamber. The result is shown in the RIGHT photo of Figure 24. The etch profile was improved. The hole was made all the way thought the wall and wider towards the angled corner. According to the "beaver tree" test structure we made on the wafer to measure lateral etch length, the wall was etched for 27~28μm in the lateral direction.

Note that the isotropic etch test was done on test wafers. Therefore the etch profile in the photos shows large cuts at the bottom of the inside walls due to lack of oxide etch stop that a SOI wafer would have on the bottom.

Dry film resist process development

The major effort we made to be able to cover our valve structures from succeeding electroplating seed layer deposition was to use 40μm thick dry film resist (DuPont FX940) instead of 15μm thick dry film resist.

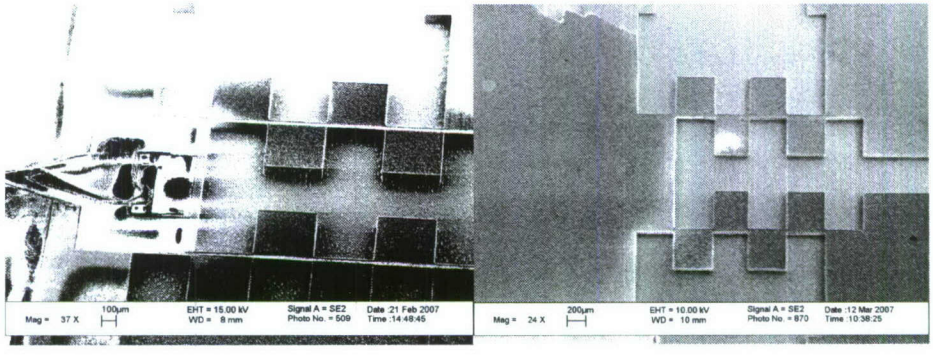

Figure 25: (LEFT) 15 μm dry film resist after oxide and Si etch
(RIGHT) 40 μm dry film resist after oxide and Si etch

The problem with 15μm DFR is that even though it can cover up the deep trenches and steps, like our 100μm deep valve features, until litho process, the film can be broken and underneath features can be exposed while going through certain etching tools. After etching the remaining 2~3 μm of oxide and 100 μm of Si, we found that 15 μm dry film resist was severely damaged. (LEFT photo of Figure 25) It seemed that combination of heat and vacuum does the most damage, as we observed a lot of broken parts of the resist film after the wafer went through LAM2 oxide etcher.

Having experienced those problems with the 15 μm film, we tried a 40 μm film. The result is shown in the RIGHT photo of Figure 25. After the oxide and Si etches, the film did not break so badly and kept valve features covered underneath. The measured film thickness after oxide and Si etches was approximately 15 μm. (The measured film thickness after development is 35 μm. The measured etch selectivity of the film against oxide in LAM2 is approximately 1:1, and the measured etch selectivity of the film against Si in STS is approximately 1:7.

Here are some tips for using dry film resist.

- Use hand-iron to laminate the film on wafers. An office laminator can break weak features on a patterned wafer, such as suspension legs, and can push the film too hard that it may cookie-cut the film against holes on a patterned wafer.
- Use DI water spray and hand-roller to avoid wrinkling/bubbling of the film while applying it on a wafer
- Use higher end of vendor's recommended exposure dose (125 mJ/cm^2 for FX940) or even overexpose. It gives better adhesion of the film.
- Agitate wafer well with tweezers while hand-developing.
- Be careful with blow drying a developed wafer immediately. It can blow away pieces of resist.
- Avoid unnecessary process with brutal vacuum or heat if possible. (e.g. Technics-c descum)

For the detailed recipes of the integrated process, please refer to Appendix1.

Electro-deposition

1) Growth of Nickel Iron film

Growth of nickel iron film has been investigated with time variation of two hours to twenty hours while current density has been fixed at 20mA/cm^2 (Figure 26). The electroformed step height of each test structure has been measured from silicon surface to electroplated surface, and this measured step height has been subtracted from a depth of test structures (100 μm) to calculate the thickness of deposited nickel iron. Low current density has been utilized to increase surface uniformity despite it decreases deposition rate. It has been shown that the deposition of 100 μm nickel iron film is achieved after twenty hours of electroplating. For several samples, there is some slow deposition rates (deposition times of 14, 16 and 18 hours). It is postulated that there was poor contact between the electrode and the samples in these tests as well as other

potential issues. Further, it is speculated that due to different locations of the samples in the electroplating bath, and width variations of a tether on test structure led to the low plating rates in these samples. Fifteen samples are parallel connected on a common cathode with even space, and the samples cover half length of electroplating bath (25cm). It is possible some area of the electroplating bath experiences less incoming flux of nickel iron, and produces low film deposition. This issue can be resolved by pumping of electrolyte with a multi-holes nozzle as well as pulse plating. In the former approach, a pump will constantly circulate electrolyte on the bath, and a multi holes nozzle in front of samples will disturb the incoming flux line, and make it uniform. These methods permit uniform incoming flux to the samples. The width variation of tether determines resistance of the test structure. Even though current density is fixed as 20mA/cm2, a potential of each sample is varied. This issue can be resolved with electroplating of samples with same width. A pump with a multi-holes nozzle will be adapted in the electroplating system, samples, which have uniform tether width, are electroplated to fully investigate effects on the film growth.

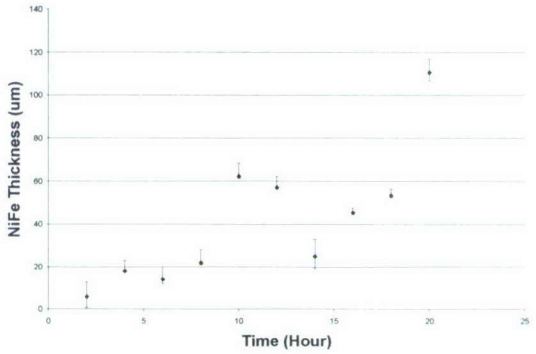

Figure 26: Deposited nickel iron film thickness against various deposition times with a current density of 20mA/cm^2

2) Surface Roughness of electroplated film

One possible reason for the surface roughness is that unwanted small nickel pieces pass through a sacrificial nickel basket and stick to the surface of electroplated structure. As shown on Figure 8, the basket has large holes (5 mm), and it is easy to escape tiny nickel pieces through the holes. Fine metal mesh, therefore, has been applied to wrap around the basket to filter and prevent the escape of small nickel pieces (Figure 27).

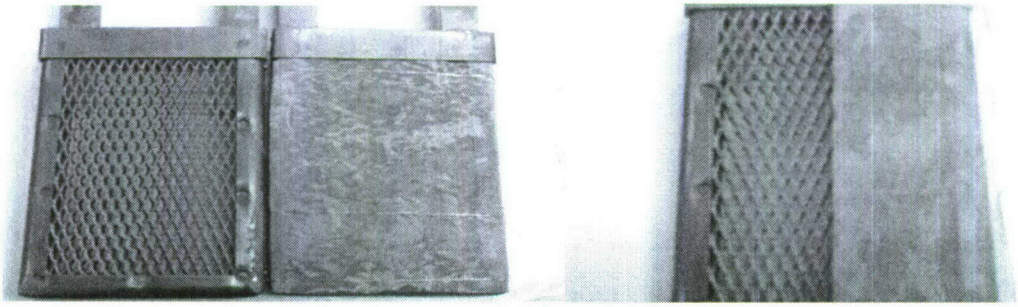

Figure 27: Fine metal mesh has been applied into the sacrificial nickel basket to filter debris.

The uniformity of the deposited film has been investigated, and thickness variations of the deposited film are shown Figure 8. The thickness of deposited film varies from the measured

average thickness, and the variations are between -5 μm and +7 μm. Unevenness of surface hampers the performance of the actuator since magnetic flux density on under-electroplated parts is lowered due to voids. Low current density (20 mA/cm^2) and the fine metal mesh around the sacrificial nickel basket did not help to improve surface roughness. Currently, a process of adapting electro-polishing into the electroplating system is ongoing. Electro-polishing will also help decrease surface roughness.

3) Electroforming Edge Growth

Electroplated film profiles of a simulated armature (A) and a tether (B) are measured to investigate edge and corner growth on test structures. A simulated armature has constant width of 3mm and tether widths are varied from 100um to 1mm (Figure 28).

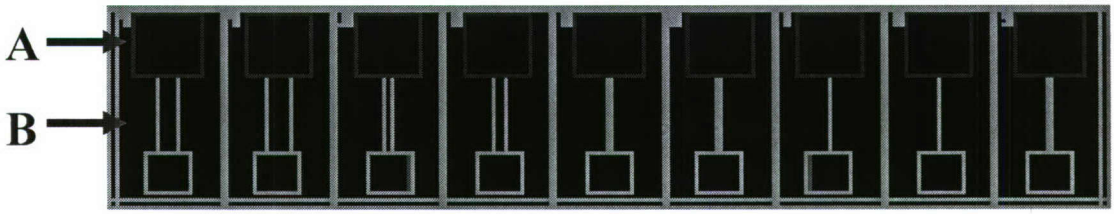

Figure 28: A simulated armature (A) and Tether (B) on the test structure

A cross-section profile of a simulated armature has been measured and plotted in figure 29 (The figure shows only half of the profile due to symmetry of film deposition, and red lines stand for a step of the test structure). Edge growth on the simulated armature shows height of 170um, and width of 400um while the film deposited to 100um on the structure. The height of this edge growth is greater than electroplated thickness on the armature and its width is four times wider than the armature thickness.

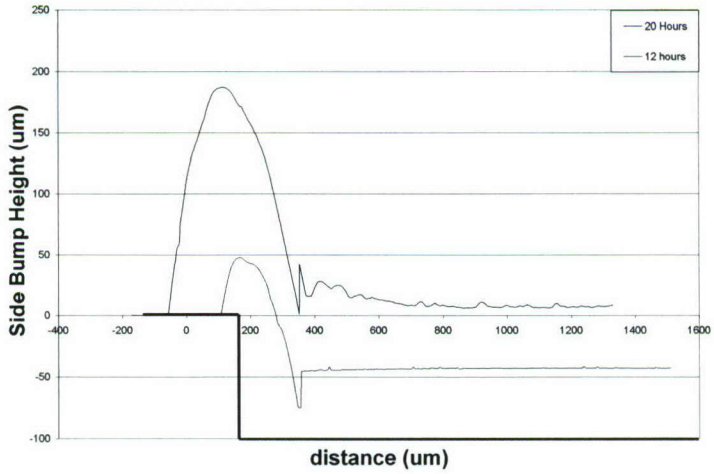

Figure 29: Side bump height growth against deposition time

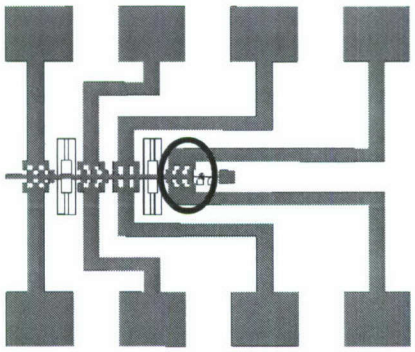

Figure 30: Width of edge growth will merge the armature with flux guides, and the armature will not actuate effectively.

The width of this edge growth (400um) after 20 hours of electroplating is unacceptable to be accommodated to the actuator design because without altering the electroplating process, the armature and flux guides will be connected by the width of these edge growth, and the connection between armature and flux guides will prevent the armature actuation (Figure 29). These edge growths are required to be controlled and either chemical mechanical planarization or electropolishing methods will be adapted to improve these plated profiles.

A cross-section profile of a tether has also been measured and plotted in figure 31. The tether width is 500 μm, and it is close to width of fingers on the proposed actuator (400 μm). The profile shows that the edge growth is up to 27 μm high and spread 100 μm wide while 25 μm of the film has been deposited after 8 hours of electroplating. After 20 hours of electroplating, however, these edge growths have a very large height and width and actually merge together. A stylus of a step height measure instrument cannot reach the valley of a tether as the diameter is greater than the width of the plated trench, and therefore unable to measure film thickness on the sample with 20 hours of electroplating.

The electroplated corners (edge growths) on a tether indicate that fingers on the actuator will be connected and there will be no fingers after electroplating in the current, simplified approach. Therefore, it is required to control this corner growth.

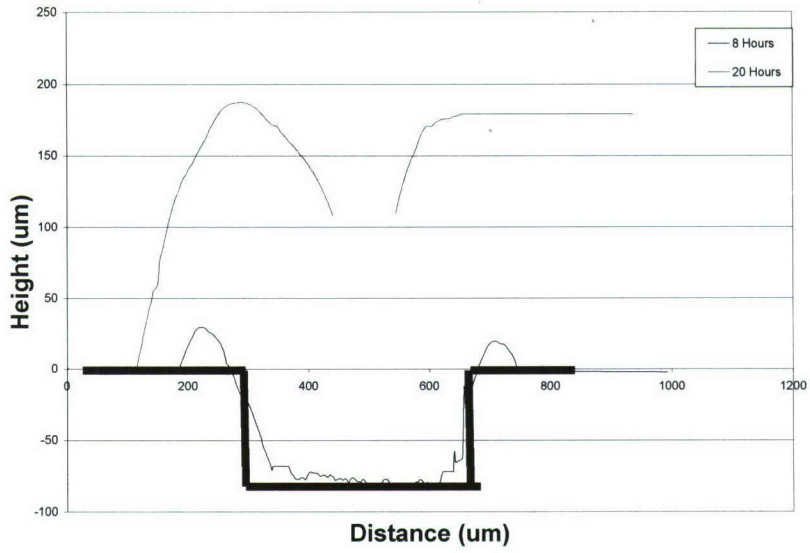

Figure 31: Side bump growth on a tether, which is simulated to electroplated fingers on the actuator, of the test structure

4) New Electrodepostion Apparatus

A multi-hole nozzle (Figure 32, Left) has been fabricated with a Computer Numerically Controlled (CNC) machining tool. The nozzle is installed in front of an electrolyte pump to improve circulation of electrolyte and surface uniformity by agitation. In addition, a wafer holder has been machined to adapt electroplating of a whole 4" wafer (Figure 32, Right). The holder also guarantees constant location of samples in an electroplating bath for test runs and provides consistency of experimetal variables. Both the nozzle with an electrolyte pump and the wafer holder are installed into the electroplating bath, and are shown in Figure 33.

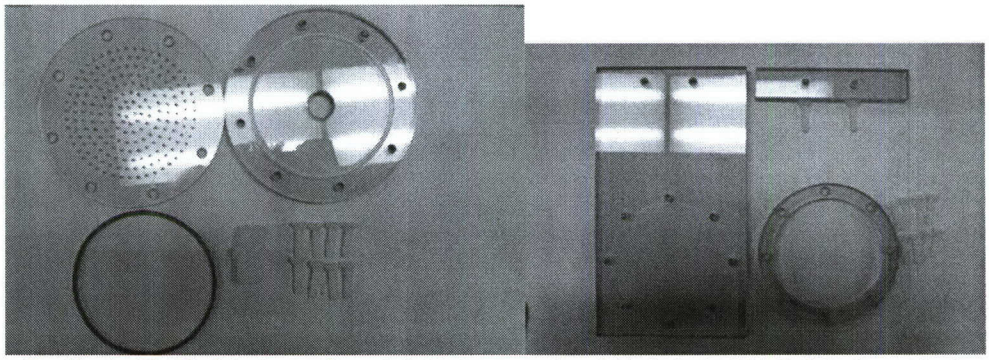

Figure 32: (Left) A CNC fabricated multi-Hole nozzle, (Right) A CNC fabricated electroplating wafer/sample holder

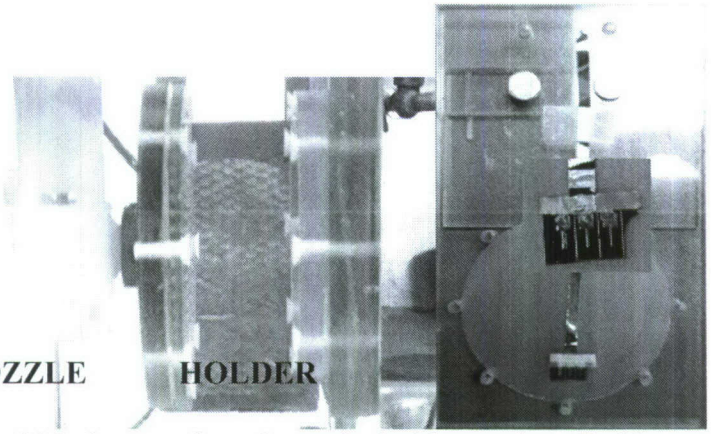

Figure 33: Left- A multi-holes nozzle and a wafer holder are installed into an electroplating bath, Right- A wafer holder with an electroplated sample.

5) Rotating Disk Field line Disruptor

Previous research has demonstrated the concept of a field line disruptor. A magnetically-insulated field lens disturbs incoming current flux, and re-distributes current density on the surface of an electroplating sample. The previous research performed a FEM simulation to prove the concept (Figure 34). The simulation shows variation of the current density concentration on the surface of trenches. Trenches without a field lens, which are located on far right side on Figure 8, receive high concentration of the incoming flux on the edge of surface. On the other hand, trenches with a field lens, which are located middle of figure 8, receive less concentrated incoming flux due to field line concentration disruption of a field lens. Trenches with a field lens, however, exhibit a decreased deposition rate comparing with the former because of lower concentration of incoming flux on the surface.

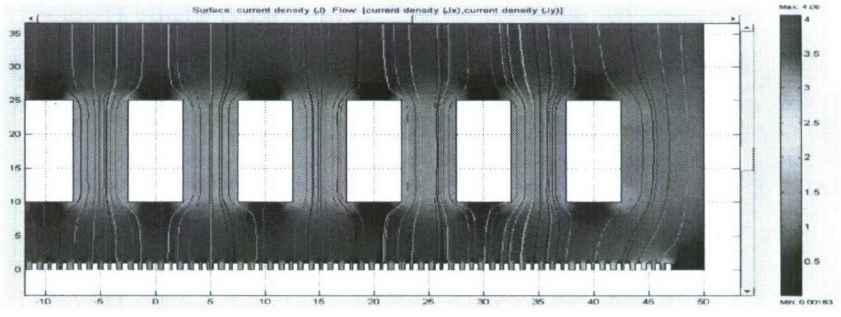

Figure 34: FEM simulation of current density concentration on trenches with a field lens

The rotating disk field line disruptor has been designed and fabricated to accommodate an advantage of a field lens while it overcomes its disadvantage. A non-conductive multi-holes disk rotates around a shaft, which is connected to an electrical motor by a V-belt, and the disk opens/blocks incoming current flux on the electroplating sample to reduce current density concentration at the edge of trenches (Figure 35). Therefore, it will re-distribute incoming flux, and makes the edge of trenches to receive less concentrate incoming flux while it is not sacrificing deposition rate.

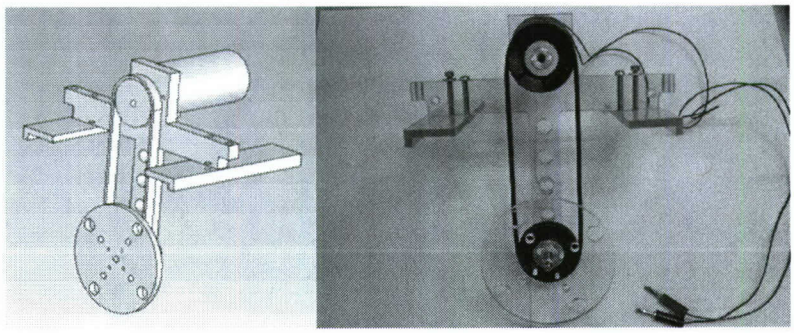

Figure 35: Rotating disk field line disruptor

6) Side Bump Growth Control

A severe side bump growth on the surface of a device layer is speculated to be an effect of vertical silicon side walls on trenches. After 100 μm of silicon deep reactive iron etching step, bare silicon is exposed on side wall of trenches. The semi-conductive silicon side walls become conductive during the electroplating process, and side bumps are grown over the surface. In order to electrically-insulate bare silicon side walls from electrolyte, conformal deposition of chemical vapor deposited (CVD) low temperature oxide (LTO) has been performed onto test structure samples, covered trench sidewalls with 0.8 μm of LTO (Figure 36-a). After deposition of LTO, photo-resist is re-deposited, and patterned for seed layers deposition (Figure 36-b). Seed layers are deposited on top of photo-resist and the bottom of the trench with an E-beam evaporator (Figure 36-c). The E-beam evaporator has been chosen since it provides the most directional deposition of seed layers, and it minimizes deposition of seed layers onto sidewall. Lift-off process has been performed to remove unnecessary seed layers on top of surface (Figure 36-d).

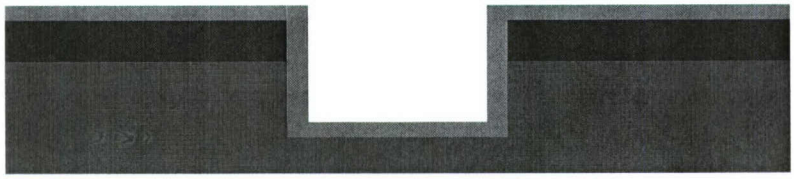

Figure 36-a: conformal Low Temperature Oxide deposited by a chemical vapor deposition furnace after 100μm Si etching process

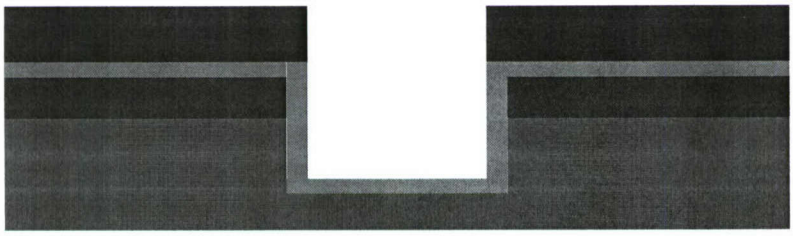

Figure 36-b: Sacrificial photo-resist deposition for lift-off process

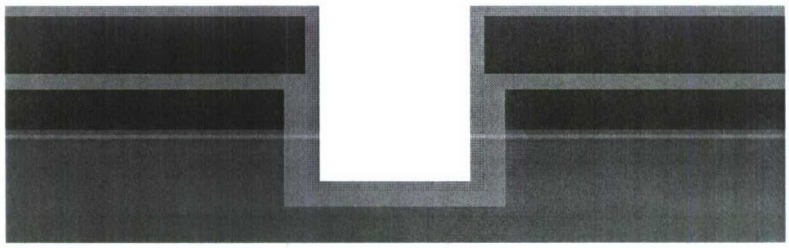

Figure 36-c: Seed layers (Cr/Cu) deposition

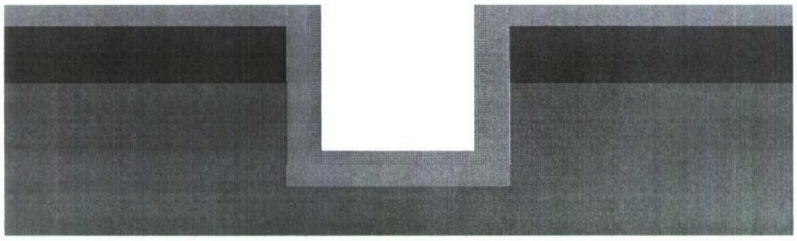

Figure 36-d: Lift-off process to remove unnecessary seed layers on device surface

Thick Dry Film Resist (40 μm) has been deposited on top of surface, where seed layers are deposited, and patterned (Figure 37-a). The dry film resist is used to prevent side bumps growth by hiding edges of seed layer deposited sidewalls (Circles on Figure 37-a), which experience the highest current density concentration during an electroplating process. In addition, thick dry film resist prevents deposition of NiFe onto surface of the device layer, and allows thin deposition of electroplated Nickel Iron (NiFe) to vertical walls of dry film resist (Figure37-b). The thin vertically deposited NiFe can be easily snapped-off after lift-off process of sacrificial dry film resist (Figure37-c).

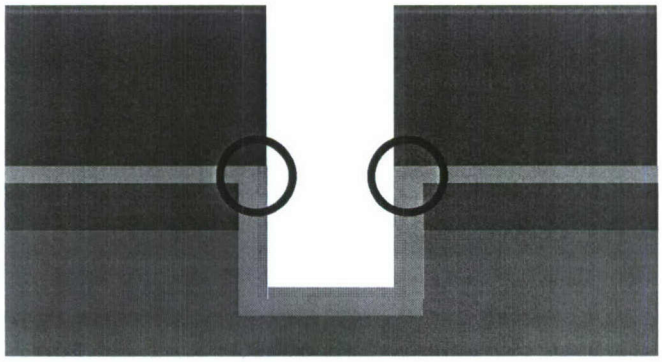

Figure 37-a: Thick Dry Film Resist (40μm) Deposition onto seed layer deposited device surface

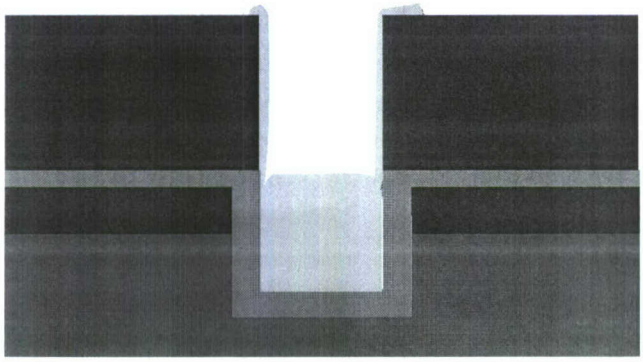

Figure 37-b: Electro-deposition process of Nickel Iron

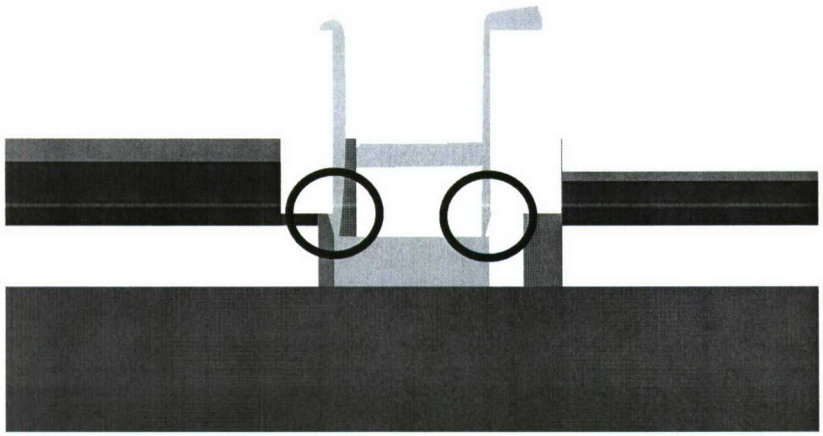

Figure 37-c: Lift-off process of Dry Film Resist, and snap-off residual NiFe

7) Surface Uniformity

Surface uniformity has been improved with a multi-holes nozzle with an electrolyte pump. Agitation of electrolyte with a nozzle and a pump removes trapped hydrogen bubbles successfully on the surface of electroplated sample and creates smooth surface (Figure 38, Left). Surface roughness has been determined as less than 5μm variation along the surface. The rotating field line disruptor demonstrates bubble-trapped surface, and surface roughness varies more than 20μm (Figure 38, Right). It indicates a multi-holes nozzle with a pump demonstrates superior surface profile over the rotating disk. Uniform surface of electroplated samples with the nozzle is due to direct impingement of electrolyte onto the surface of samples. Direct impingement of electrolyte prevents/removes any contact of hydrogen bubbles, which are due to chemical reaction between Nickel and electrolyte, from the surface. The disruptor, however, creates only rotary motion around the close surface of the sample, and it was not able to prevent attachment of hydrogen bubbles into the surface. It was not able to install both the nozzle with the disruptor because of space confinement of an electroplating bath. The disruptor will be modified to accommodate the space limitation, and tested with the nozzle.

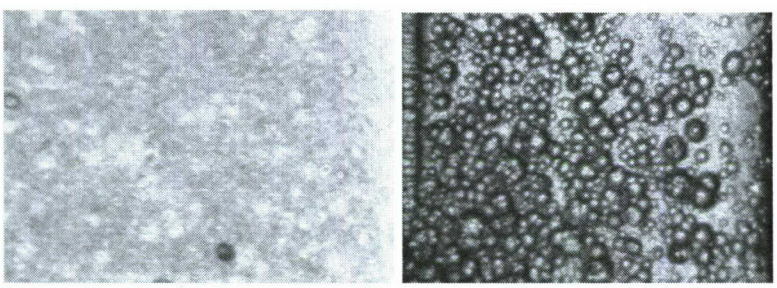

Figure 38: Left- Smooth surface created by a multi-holes nozzle with an electrolyte pump. Right- Rough surface created by a rotation disk field line disruptor

8) Side Bump Growth Control Result

Deposition of a dry film resist has been prevented side bump growth of NiFe onto the surface of samples. Comparing with the result of NiFe deposition profile without a DFR (Figure 39, Left), the sample with DRF (Figure 39, Right) demonstrates that the side bumps have been diminished, and vertical edges of trenches are shown after an electroplating process. The dry film resist has been removed after NiFe deposition by acetone, and residual electroplated NiFe over dry film

resist has been removed by tweezers. Dark area inside the trench shows low amount of NiFe deposition, and resulted from a misalignment between seed layer surface and dry film resist (Figure 39, Right Circle). This misalignment between seed layers and the dry film resist, however, provides suggests the possibility of a new dry film resist mask design, which allows intentionally over-covered the structure to avoid side bump growth on the surface of device layer (Figure 40). Both effects of perfect alignment and over-covered mask are investigated and reported in next quarter.

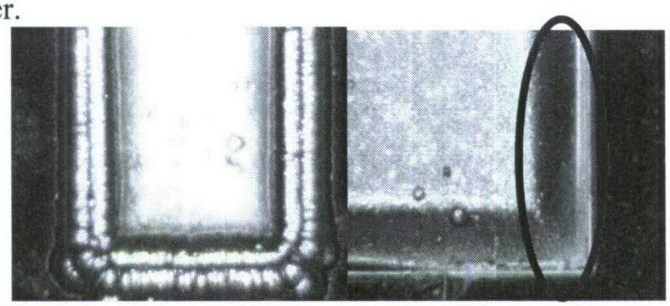

Figure 39: Left- Nickel Iron deposition without dry film resist, Right- Vertical sidewalls with dry film resist

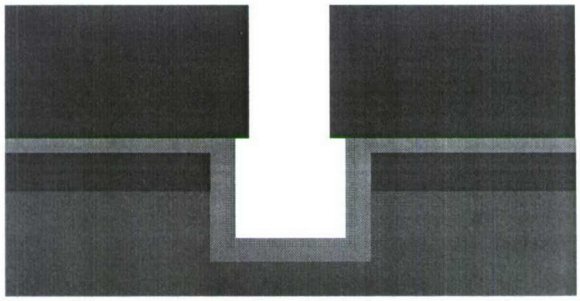

Figure 40: New design of dry film resist mask which intentionally over-covered the structure to prevent side growth of NiFe on edge of the trench

9) Material Composition of Electroplated Samples

Material Composition of electroplated NiFe sample has been measured with a SEM EDX machine. As expected, Nickel and Iron shows close to 80:20 weight percentile composition ratio (Figure 41). Oxygen and Sodium are shown on a composition graph because of oxidation and metal contamination of seed layer due to ambient surroundings.

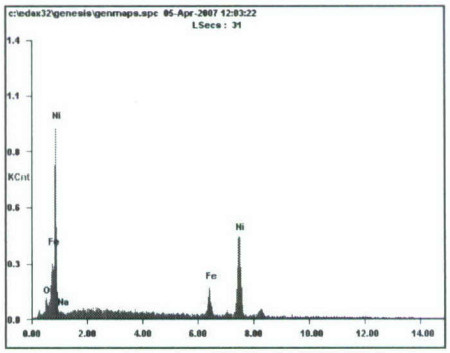

Figure 41: Material composition of electroplated Nickel Iron sample

10) Over-covered dry film resist

It has been reported that a misalignment between seed layers and dry film resist provides suggests the possibility of a new dry film resist mask design, which allows intentionally over-covered the structure to avoid side bumps growth on the surface of device layer (Figure 42). Scanning Electron Microscope (SEM) images have been taken to investigate feasibility of the over-covered dry film resist. Figure 42 shows a profile of a cross section before removal of a dry film resist. Silicon trench is filled with NiFe, and side-bumps have been formed from the edge of sidewalls. Left side of the figure demonstrates the over-covered dry film resist, which covers the edge of side wall. The over-covered resist demonstrates that it prevents growth of a side bump over silicon trench area, and the feasibility of the over-coated resist technique has been achieved.

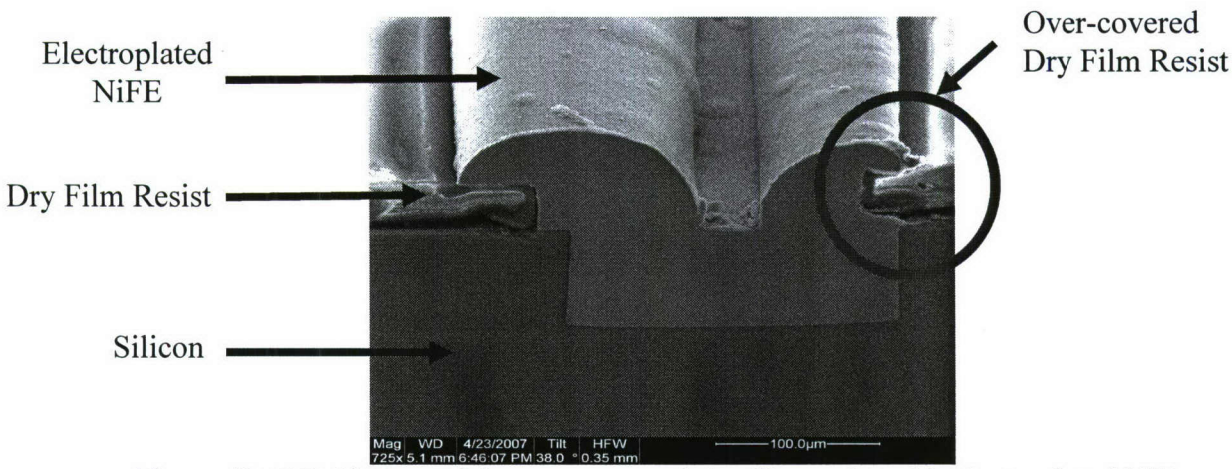

Figure 42: SEM image of the over-covered dry film resist with electroplated NiFe

After electroplating process, the film resist has been removed by lift-off process, and undesired NiFe above the film has been snapped off by tweezers (Figure 43). SEM images demonstrate that over-deposited NiFe has been successively removed. This technique has been implemented into the design of the second mask for the optimized actuator, and the mask has been fabricated.

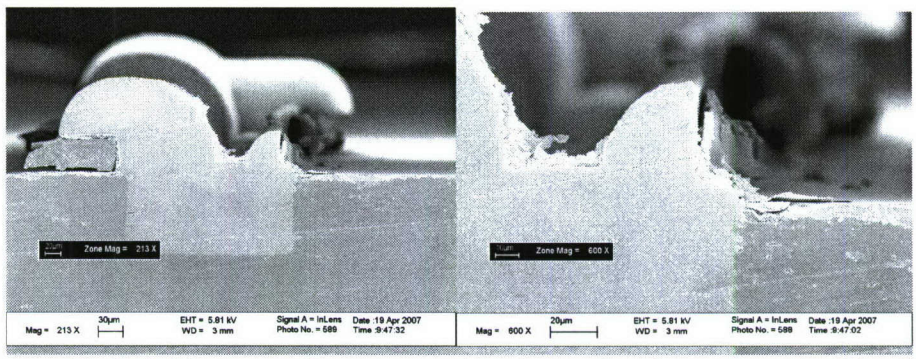

Figure 43: SEM images of an electroplated sample after removal of the film

B-2 Coil/Circuit

The NiFe parts for the actuator test structure are cut from 100 micron and 1mm thick NiFe sheets using wire-EDM. The smallest feature of a part is 400 μm. The advantage of making NiFe parts out of sheets is that it has potential to significantly lower the manufacturing cost of the device for mass production. The electro disposition process requires long deposition time that reduces the throughput and current-control equipment for each electro-deposition piece. On the other hand, the precision machining and pick-and-place assembly can be done in cost-effective manner with state-of-art mass production techniques used by the industry.

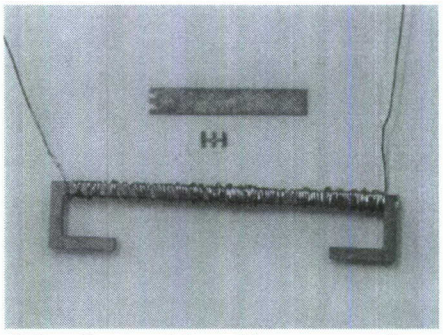

Figure 44: NiFe parts and the flux guide with surrounding coil made by wire-EDM

The parts are pick-and-placed by hand on the testing-platform wafer and attached using photo resist. Photo resist robustly stands the following releasing step in HF.

E. Testing

C-1 Coil/Circuit testing with a dummy motor

The actuator testing platform was assembled and the actuator was successfully moved being applied the current controlled by Keithley 2500.

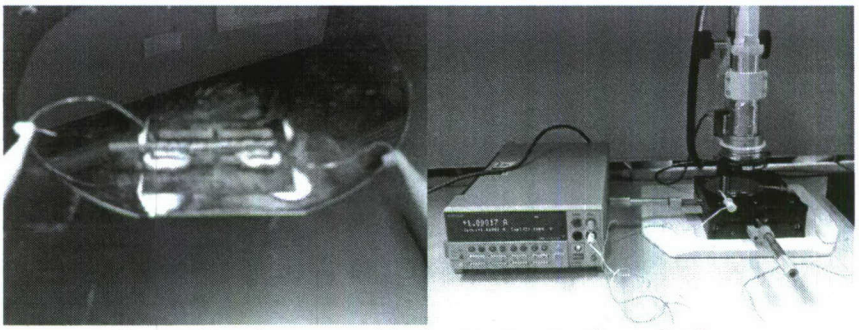

Figure45. The assembled actuator testing platform

With input of 1A current through 300 turns on the flux guide, the actuator showed 0.97 mN force output.

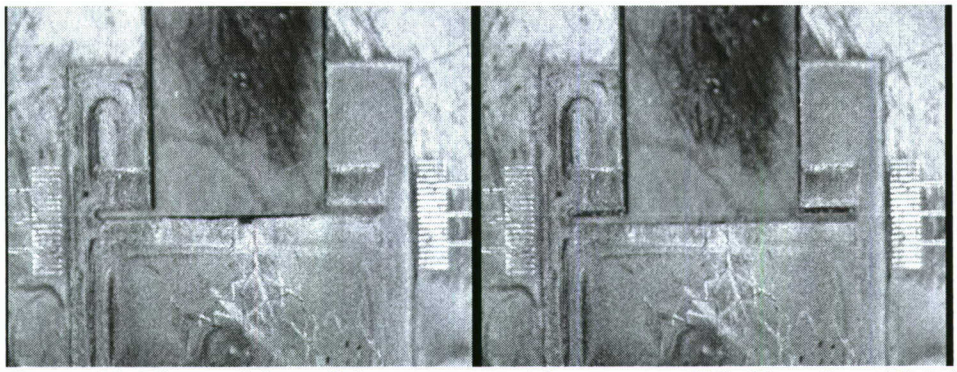

Figure 46: The position of the actuator with current off (left) and on (right)

C-2 Prototype Valve Testing

Two different encapsulation methods are adapted for testing the system performance depending on driving pressures; 1) a dynamic mode for low driving pressure and 2) a static mode for high operational pressure. The dynamic mode denotes that the fluid is regulated by active motion of the MEMS EM linear actuator. In order to generate the electromotive force on the actuator, CNC machined yokes and coils (30 AWG) are embedded into the encapsulation. The CNC fabricated polycarbonate housing accepts electromagnetic components and fluidic connections for the inlet and exhaust (Fig. 46, (A)). The faces of the upper and lower housing are secured by screws with a face seal gasket. On the other hand, static mode decouples the electromagnetic actuation from the valve characterization (Fig. 46, (B)). In other words, the macro-scale electromagnetic components are detached from the microfabricated valve system, and the gate positions are fixed during the characterization. A microscope glass slide has been bonded on top of the valve system to encapsulate the microchannel. A thin layer of strain gauge adhesive (VISHAY, M-Bond 610) has been applied to bond the slide and the silicon surface. The glass slide has been drilled for inlet and exhaust before the bonding process, and port connectors (LabSmith, C0400-Ultem) are attached on a top glass surface in order to accept and secure the tubing. The static test has been performed to minimize fluidic leakage from the microchannel to accurately measure the outcome mass flow rate with respect to the valve gate positions on high driving pressure regions.

The fluidic characterization for the dynamic and static modes has been performed. The positions of gate and driving pressures have been varied, and corresponding mass flow rate and pressure drop across the valve are measured. Deionized water has been utilized on fluidic characterization. In addition, the fluidic resistance has been estimated from the experimental measurements.

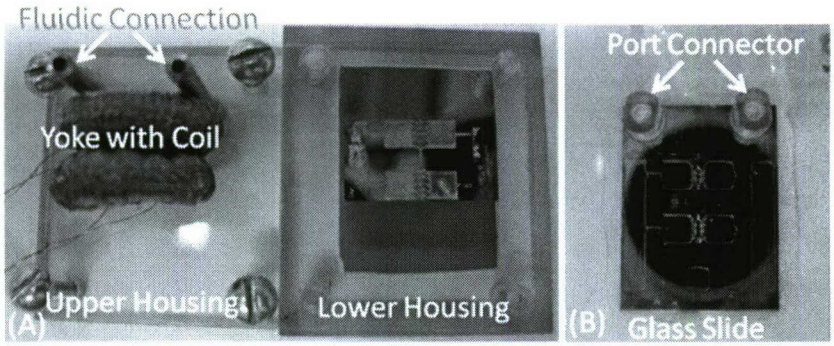

Fig. 46: Two different encapsulation methods have been implemented to characterize the MEMS valve system. (A) Dynamic mode and (B) Static mode.

Dynamic Mode

The MEMS EM linear actuator has been energized with the electromotive force of 60 ampere-turn (AT), and the energized actuator regulates the flow by varying positions of the gate. With constant driving pressure of 1.4 kPa, the valve system is able to regulate the fluid stream and produces three distinct regions of mass flow rate (Fig. 47). The MEMS EM actuator has varied the gate positions during the experiment, and the corresponding variation of mass flow rate has been measured. The valve system has delivered the averaged mass flow rate between 0 and 0.5 mg/sec with respect to the gate positions. At the open gate position, the maximum flow rate is determined as 0.5 ± 0.02 mg/sec. The half open gate position allows the flow rate as 0.25 ± 0.02 mg/sec, and the closed gate position induces insignificant leakage.

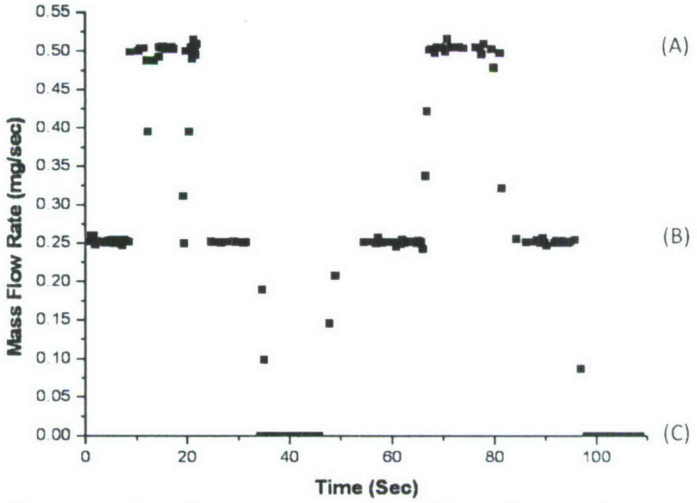

Figure 47: The mass flow rate has been measured with various valve gate positions at driving pressure of 1.4 kPa. The graph demonstrates three different mass flow rate regions, which are corresponded to the distinct gate positions. (A) Open, (B) Half-open and (C) Closed gate position.

Static Mode

The MEMS fuel delivery system with high driving pressure regions has been characterized with the static mode. The static tests have been designed to minimize not only leakage flow from the microchannel, but also dead volume of the package by decoupling the electromagnetic components from the valve system. The decoupling of valve actuation from the valve system removes required clearance between the armature and the upper package plate. The clearance is needed for the dynamic mode to remove friction between the moving armature and the encapsulation. In addition, the package design becomes simple by removing the electromagnetic components, and it minimizes dead volume, which serves as a fluidic capacitor. Furthermore, utilization of the flat glass slide, which has sub micron roughness, as the top encapsulation rather than the microscopically uneven polycarbonate top plate provides uniform contact between the silicon microchannel and the microscope slide to offer superior face sealing. With the static mode, the planar valve is able to handle high pressures with the minimum leakage between the microchannel and the encapsulation.

The static tests are performed to characterize the MEMS liquid fuel delivery system for high pressure operation with various driving pressures. The driving pressure has been varied from 14 to 98 kPa with an increment of 14 kPa while three separated MEMS valves are prepared with three gate positions. It is determined that mass flow rate has been increased with the increase of

driving pressure. The averaged mass flow rates are varied between 0 and 9.12 mg/sec depending on the gate positions (Fig. 48). The variations of the mass flow rate at the open, the half open and the closed gate position are determined as 1.21 to 9.59 mg/sec, 0.72 to 4.73 mg/sec, and 0 to0.09 mg/sec respectively.

Fluidic resistance has been estimated for the high driving pressure regions. The fluidic resistance is defined as a ratio of pressure drop across the valve system to delivered volume flow rate and indicates reluctance of flow passage through the valve system. It has been determined that the fluidic resistance for the closed gate position has approximately two orders of magnitude higher than the half open and open gate positions (Tab. 12). Furthermore, the fluidic resistance ratio (K) has been calculated for both the half open and the open gate positions, and the ratio is determined as 88 and 182 respectively. In other words, when the valve is closed, the system allows approximately one hundred times less amount of the flow to pass the microchannel comparing with the open gate positions at the given driving pressure.

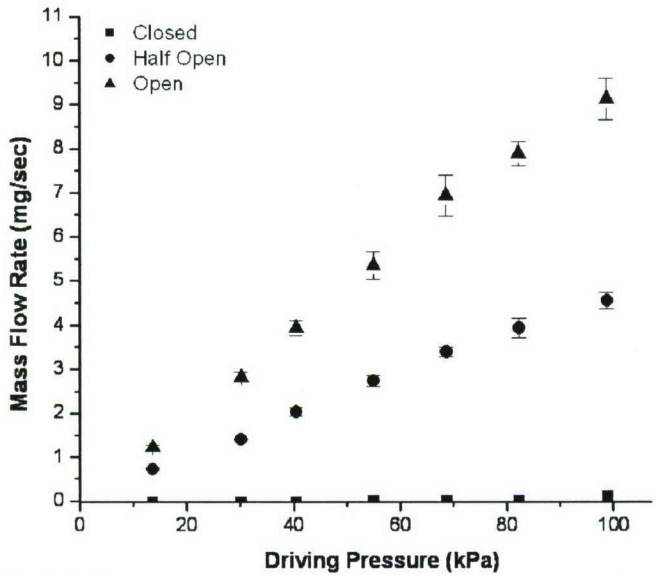

Figure 48: The MEMS fuel delivery system is able to deliver up to 9.59 mg/sec of mass flow rate without major leakage. As the driving pressure increases, the open and half-open gate positions yield increased mass flow rates while the closed gate position prevents leakage flow. Leakage for the closed gate position has been observed when the driving pressure becomes greater than 100 kPa.

Tale 12: The fluidic resistances and fluidic resistance ratios have been estimated for the static mode. Both half open and open gate positions produce the fluidic resistance ratio as approximately an order of 102.

Gate Position	Fluidic Resistance (Ns/m^5)	K
Closed	$1.83x10^{15}$	-
Half Open	$2.08x10^{13}$	$8.83x10^{1}$
Open	$1.00x10^{13}$	$1.82x10^{2}$

The MEMS liquid fuel delivery system has provided feasibility of the fuel delivery for small-scale combustion power systems. The system has delivered up to 9.5 mg/sec of deionized water, and insignificant leakage has been observed when the valve is closed. This MEMS liquid fuel

delivery system would be able to deliver 428 Watts of chemical energy into the portable power with assumption of typical liquid hydrocarbon energy density as 45 MJ/kg. In addition, the fluidic resistance ratios for open and half-open gate positions have been estimated as an order of 100. This ratio is adequate for fuel regulation applications for engines where 100:1 flow ratios are typical. Furthermore, the MEMS fuel valve system has demonstrated metering operation, which varies amount of flow with respect to the gate positions, rather than check valve operation, which only allows either closed or open positions. Precise control of fuel is a critical factor of successful development of small-scale engines because the engines only produce the maximum power output at narrow region of stoichiometry between fuel and oxidizer.

Appendix I: Process Flow

Equipment	Wfr#	Notes1	Notes2	Date Comp
Sink6		clean, 10:1 HF dip		
Tystar12		6 um deposition, 06:40:00 dep time		
Tystar3		N2 anneal, 1000 C 01:00:00 dep time		
Nanospec		Measure oxide thickness, report in notes		
VWR Oven		Dehydrate, 120 C 00:10:00 (include 2 dummies for exposure tests)		
Sink5		HMDS Mist Coat 00:05:00 (incl dummies) (make sure wafers cool before spinning PR)		
Svgcoat1		~7 um g-line, 3x(coat #4, bake #1) (incl dummies)		
KSaligner		Oxide Mask, soft contact (12.0 sec exposure @ 21.2 intensity) 254 mJ		
Svgdev		g-line 25% overdevelop, 2x(dev #5, bake #7)		
VWRoven		Hardbake, 120 C 02:00:00		
Lam2		Oxide Etch SiO2MON ~ 11x(00:01:30) etch steps wait until 15C, ¼ spin between runs look for oxide to clear in trenches		
Sink5		PRS-3000 strip 00:15:00, rinse, spin dry		
Technics-C		Ash, 300W, 00:07:00		
VWR Oven		Dehydrate, 120 C 00:10:00 (include 2 dummies for exposure tests)		
Sink5		HMDS Mist Coat 00:05:00 (incl dummies) (make sure wafers cool before		

		spinning PR)		
Svgcoat1		~7 um g-line, 3x(coat #4, bake #1) (incl dummies)		
KSaligner		Resist Mask, soft contact (~45 sec exposure) Overexpose a lot. Thick resist can be built up by spin around fine oxide patterns of new oxide mask.		
Svgdev		g-line 25% overdevelop, 2x(dev #5, bake #7) g-line half develop Up to 2x (dev #4, bake #7) Check fine features with microscope		
Hotplate		Apply cool-grease on p-type handles 50C		
WaferBond		Align, press wafers together using tekwipe-protected tweezers. Press wafer with a weight protecting the surface with tekwipe		
Oven		Bake 70C 00:10:00		
Technics-C		Pumpdown vacuum check 00:10:00		
STS		JFRANK3A 00:45:00 for ~80 um etch Measured etch rate = 1.8 um/min @ HBC 2.15 Ensure chamber is warm with cond3 run	HBC SF6=123.3 C4F8=148.2 O2=12.3 Pressure etch=18 mT Pressure pass=15mT	
ASIQ		Etch depth measurements, Record in notes		
Nanospec		Lip oxide thickness Record in notes		
Spinner 1		Acetone rinse, while spinning May need to drip PRS-3000 to remove all PR	The resist may not be completely ripped off and prevent the wafer from etching in STS. If that happens, take off handle wafer and piranha clean the wafer.	
Technics-C		Ash, 300W, 00:04:00		
Technics-C		Pumpdown vacuum check 00:10:00		
STS		JFRANK3A 00:3500 for ~40m etch Measured etch rate = 1.3 um/min @ HBC 2.6 Ensure chamber is warm with cond3 run. Aim for 40 micron etch. Compensate for oxide thickness.	HBC SF6=123.3 C4F8=148.2 O2=12.3 Pressure etch=18 mT Pressure pass=15mT	
ASIQ		Etch depth measurements, Record in notes		
Nanospec		Lip oxide thickness Record in notes		

Old lab sink		Handle Wafer Debond with acetone 04:00:00, paper slice		
Sink8		Piranha Clean + HF dip (~5 seconds)		
Sink7		Isotropic Silicon wet etch for 2 micron undercut. Monitor etch rate closely. Etch rate depends on substrate doping levels. Minimum 1 full bottle of etchant. Ensure all wafers are exposed equally to solution when being mixed. Wafers that are more exposed to vigorous fluid flow etch faster.		
Leo		Inspect sidewalls, etch back		
Tystar3		1.0 um Wall oxide growth 1050 C, 03:06:00		
Lam2		Trench Bottom Oxide Removal Adjust gap to 0.5 cm, pressure to 3.2 mTorr. ~7 x 00:01:00 cycles Rotate wafers ¼ turn each run		
Nanospec		Lip oxide thickness Record in notes		
Hotplate		Apply cool-grease on p-type handles 50C		
WaferBond		Align, press wafers together using tekwipe-protected tweezers. Press wafer with a weight protecting the surface with tekwipe		
Oven		Bake 70C 00:10:00		
Technics-C		Pumpdown vacuum check 00:10:00		
STS		JFRKISO3 00:07:00, then check test structures Ensure chamber is warm with cond3 run		
Old lab sink		Handle Wafer Debond acetone 04:00:00		
Sink8		Piranha Clean		
VWR Oven		Dehydrate 00:10:00, 120C		
Sink5		HMDS 00:05:00 Wait for wafers to cool before spinning.		
Spinner1		SJR-5740. Large dropper full Slow spin until spread out 00:00:30 at 2 krpm 00:04:00 softbake 120C HOTPLATE		
Ksaligner		BackSide, 00:00:20 seconds		
Sink5		Hand develop, MP DEV, 00:05:00		
VWR oven		Hardbake 120C 01:30:00		
Lam2		SiO2MON		

		13x(00:01:30) SJR-5740 may burn. Proceed.		
Sink5		PRS-3000 strip 00:15:00, rinse, spin dry		
Technics-C		Ash, 300W, 00:07:00		
Hand iron		Laminate dry film resist (Heat 4) Spray water and use hand-roller to avoid wrinkles/bubbles. Make sure to use flat surface. The wafer may break.		
KSaligner		NiFe Mask, soft contact (6.6 sec exposure @ 19 intensity, gap = 80) 125 mJ Overexpose is better.		
Sink5		Hand develop, PO_2CO_3 solution (15g PO_2CO_3 and 2L DI water), 00:03:00~00:03:20 Agitate the wafer very well with tweezers. Be careful with blow-drying. Check with microscope for clear surface		
		Stabilization/drying over night		
Lam2		Oxide Etch SiO2MON ~ 8x(00:01:00) etch steps wait until 15C, ¼ spin between runs look for oxide to clear in trenches Reduce the etch time if the resist film seems to break		
Hotplate		Apply cool-grease on p-type handles 50C		
WaferBond		Align, press wafers together using tekwipe-protected tweezers. Press wafer with a weight protecting the surface with tekwipe		
Oven		Bake 70C 00:10:00		
STS		JFRANK3A 00:60:00 for 100 um etch Measured etch rate = 1.8 um/min @ HBC 2.15 Ensure chamber is warm with cond3 run	HBC SF6=123.3 C4F8=148.2 O2=12.3 Pressure etch=18 mT Pressure pass=15mT	
Leo		Inspect bottom of trenches to check soot		